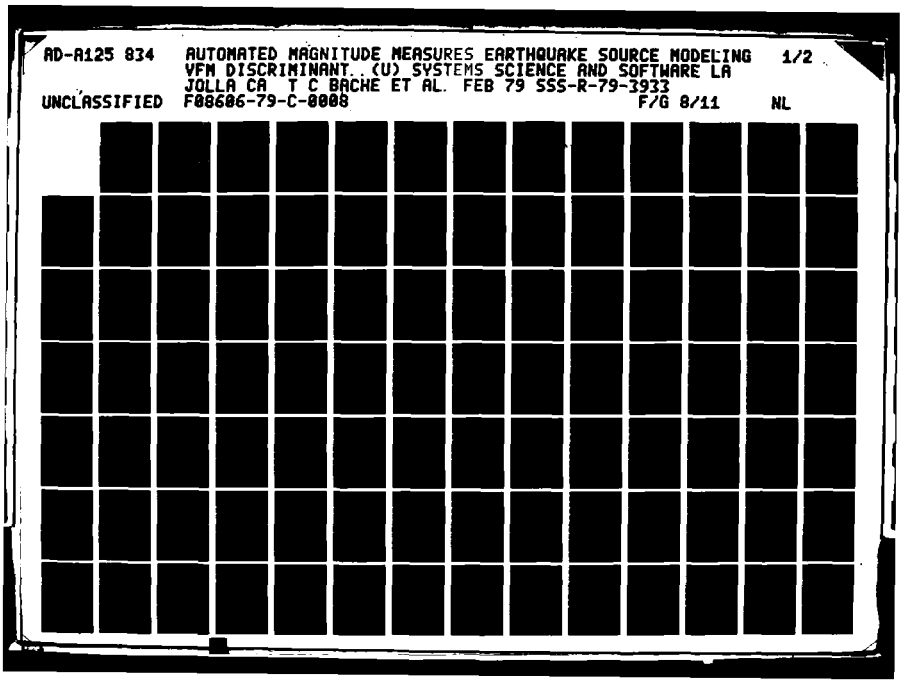
AD-A125 834
AUTOMATED MAGNITUDE MEASURES EARTHQUAKE SOURCE MODELING
VFM DISCRIMINANT..(U) SYSTEMS SCIENCE AND SOFTWARE LA
JOLLA CA T C BACHE ET AL. FEB 79 SSS-R-79-3933
1/2
UNCLASSIFIED
F08606-79-C-0008
F/G 8/11
NL

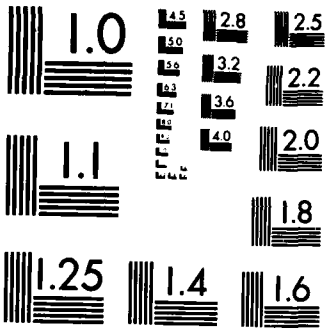

SYSTEMS, SCIENCE AND SOFTWARE

SSS-R-79-3933

AUTOMATED MAGNITUDE MEASURES, EARTHQUAKE SOURCE MODELING, VFM DISCRIMINANT TESTING AND SUMMARY OF CURRENT RESEARCH

T. C. Bache
S. M. Day
J. M. Savino

Quarterly Technical Report
For Period October 1 - December 31, 1978

Sponsored by
Advanced Research Projects Agency
ARPA Order No. 2551

This research was supported by the Advanced Research Projects Agency of the Department of Defense and was monitored by AFTAC/VSC, Patrick Air Force Base, Florida, 32925, under Contract No. F08606-79-C-0008.

February 1979

P. O. BOX 1620, LA JOLLA, CALIFORNIA 92038, TELEPHONE (714) 453-0060

UNCLASSIFIED

SECURITY CLASSIFICATION OF THIS PAGE (When Data Entered)

REPORT DOCUMENTATION PAGE		READ INSTRUCTIONS BEFORE COMPLETING FORM
1. REPORT NUMBER	2. GOVT ACCESSION NO.	3. RECIPIENT'S CATALOG NUMBER
4. TITLE (and Subtitle) AUTOMATED MAGNITUDE MEASURES, EARTHQUAKE SOURCE MODELING, VFM DISCRIMINANT TESTING AND SUMMARY OF CURRENT RESEARCH		5. TYPE OF REPORT & PERIOD COVERED Quarterly Technical 10-1-78 to 12-31-78 6. PERFORMING ORG. REPORT NUMBER SSS-R-79-3933
7. AUTHOR(s) T. C. Bache S. M. Day J. M. Savino		8. CONTRACT OR GRANT NUMBER(s) F08606-79-C-0008
9. PERFORMING ORGANIZATION NAME AND ADDRESS Systems, Science and Software P. O. Box 1620 La Jolla, California 92038		10. PROGRAM ELEMENT, PROJECT, TASK AREA & WORK UNIT NUMBERS Program Code No. 6H189 ARPA Order No. 2551
11. CONTROLLING OFFICE NAME AND ADDRESS VELA Seismological Center 312 Montgomery Street Alexandria, Virginia 22314		12. REPORT DATE February 1979 13. NUMBER OF PAGES 98
14. MONITORING AGENCY NAME & ADDRESS(if different from Controlling Office)		15. SECURITY CLASS. (of this report) Unclassified 15a. DECLASSIFICATION COWNGRADING SCHEDULE

16. DISTRIBUTION STATEMENT (of this Report)

Approved for public release, distribution unlimited.

17. DISTRIBUTION STATEMENT (of the abstract entered in Block 20, if different from Report)

18. SUPPLEMENTARY NOTES

19. KEY WORDS (Continue on reverse side if necessary and identify by block number)

Nuclear Explosion Seismology
Seismic Source Theory
Seismic Discrimination
Seismic Signal Processing

20. ABSTRACT (Continue on reverse side if necessary and identify by block number)

Brief summaries of work currently underway or completed during the period from 1 October to 31 December 1978 are given in seven sections; Source Calculations, Discrimination, Yield Determination, Small-Scale Experiments, Selected Geological Studies, Magnitude-Yield Improvements and Ground Motion Analysis.

(continued)

DD FORM 1 JAN 73 1473 EDITION OF 1 NOV 65 IS OBSOLETE

UNCLASSIFIED

SECURITY CLASSIFICATION OF THIS PAGE (When Data Entered)

20. ABSTRACT (continued)

The remainder of the report is devoted to presentation of results not previously reported from three research projects. The first is concerned with the development and testing of an automated spectral body wave magnitude called $\hat{m}_b$. The $\hat{m}_b$ is based on the spectral amplitude of the recorded signal in a narrow window in both time and frequency. For comparison to the $\hat{m}_b$, time domain m_b is computed for each recording with a semi-automatic technique in which all records are prefiltered to appear as if recorded by the same instrument. Amplitude and time measurements are made automatically during this process. The $\hat{m}_b$ algorithm is tested by application to synthetic seismograms and to HNME recordings of Pahute Mesa explosions.

The second detailed discussion is entitled, "Three-Dimensional Earthquake Modeling." Results from two finite difference simulations of earthquake faulting performed on the ILLIAC computer are summarized. In one case, the material was elastic and in the second, plastic yielding was allowed near the fault plane.

The third detailed discussion is entitled, "Discrimination Experiment." Two modifications to the MARS program used for discrimination are described. One is an algorithm for correcting for the effects of seismic noise. The second is an algorithm for averaging weighted estimates to obtain the high and low frequency magnitudes used to classify events.

TABLE OF CONTENTS

Section		Page
I.	INTRODUCTION	1
	1.1 BACKGROUND	1
	1.2 SUMMARY OF RESEARCH DURING THIS QUARTER	1
	1.3 SUMMARY OF SECTION II: "SEISMIC WAVEFORMS AND TIME DOMAIN m_b"	5
	1.4 SUMMARY OF SECTION III: "$\hat{m}_b$, AN AUTOMATED SPECTRAL MAGNITUDE"	5
	1.5 SUMMARY OF SECTION IV: "$\hat{m}_b$ FOR SYNTHETIC SEISMOGRAMS"	6
	1.6 THREE-DIMENSIONAL EARTHQUAKE MODELING	6
	1.7 DISCRIMINATION EXPERIMENT	7
II.	SEISMIC WAVEFORMS AND TIME DOMAIN m_b	9
	2.1 INTRODUCTION	9
	2.2 A SEMI-AUTOMATED TIME DOMAIN m_b	16
	2.3 HNME DATA	17
III.	$\hat{m}_b$, AN AUTOMATED SPECTRAL MAGNITUDE	23
	3.1 INTRODUCTION	23
	3.2 MARS ANALYSIS AND THE DEFINITION OF VFM	24
	3.3 DEFINITION OF $\hat{m}_b$	32
	3.4 $\hat{m}_b$ FOR HNME SEISMOGRAMS	38
IV.	$\hat{m}_b$ FOR SYNTHETIC SEISMOGRAMS	40
V.	THREE-DIMENSIONAL FINITE DIFFERENCE EARTHQUAKE MODELING	59
	5.1 INTRODUCTION	59

TABLE OF CONTENTS (continued)

Section			Page
	5.2	SUMMARY OF RESULTS.	62
		5.2.1 Comparison of an Analytic Solution	62
		5.2.2 Stress History Near the Fault. .	64
		5.2.3 Velocity History on the Fault. .	66
		5.2.4 Radiated Fields.	70
		5.2.5 Comparison to Radiation from an Archambeau-Minster Source . .	78
	5.3	DISCUSSION.	82
	5.4	RESEARCH PLANS.	83
VI.		DISCRIMINATION EXPERIMENT.	85
	6.1	SEISMIC NOISE CORRECTION.	85
	6.2	NOISE CORRECTED MEAN WEIGHTED $\bar{m}_b(f)$ ESTIMATES	90
	6.3	DISCRIMINATION RESULTS.	95
REFERENCES			96

LIST OF ILLUSTRATIONS

Figure		Page
1.	Locations of eleven Pahute Mesa events	10
2.	Relative amplitude response for two instruments used at the HNME site.	15
3.	The HNME recordings of eleven Pahute Mesa events	18
4.	The HNME recordings showing increasing source-surface travel time	20
5.	Schematic presentation of the MARS algorithm.	26
6.	Forty-eight narrow band filters with center frequencies $0.2 \leq f_k \leq 1.6$ Hz are plotted	
7.	The time domain filters are plotted for four f_k.	31
8.	For each of the HNME recordings of Figure 3 we plot log $(A_k \cdot f_k)$ and t_g versus filter center frequency, f_k.	34
9.	The HNME recordings from Figure 4 are shown with a scale indicating the limits of the t_g band used in the $\hat{m}_b$ calculation.	37
10.	The source functions for three Pahute Mesa explosions are plotted with the amplitude axis scaled to 0.02 KT while the frequency axis is scaled to 600 KT	41
11.	Construction of theoretical seismograms at HNME for three Pahute Mesa explosions.	48
12.	Comparison of synthetic and observed seismograms.	49
13.	Log $(A_k \cdot f_k)$ and t_g versus f_k for the synthetic seismograms of Figure 11	54
14.	The P + pP + P_s synthetic seismograms from Figure 11 are shown with marks indicating the t_g time band for the $\hat{m}_b$ determination. . .	56

LIST OF ILLUSTRATIONS (continued)

Figure		Page
15.	The fault configuration for the finite difference simulation and the coordinate system for describing the radiated field . . .	60
16.	Relative displacement on the fault for the elastic case	63
17.	Time histories for the stress component σ_{yz} adjacent to the fault plane, for several hypocentral distances.	65
18.	Time history of σ_{yz} adjacent to the fault plane for several azimuthal angles ϕ	67
19.	Time history of σ_{yy} along the fault plane. . .	68
20.	Slip velocity in the fault plane	69
21.	Normalized far-field P wave and S wave displacement spectra and time histories Displacements are shown at 10° intervals in θ, for ϕ = 90°.	71
22.	Normalized far-field P wave and S wave displacement spectra and time histories. Displacements are shown at 10° intervals in θ, for ϕ = 45°.	73
23.	Comparison of displacement spectra and time histories from the plastic problem with those from the elastic problem.	77
24.	Comparison of synthetic seismograms from the elastic finite difference source to those from a bilateral version of the Archambeau model	80
25a.	Typical event distributions in the $m_b(f)$ plane for event data that is not corrected for noise contamination.	93
25b.	Typical event distributions in the $m_b(f)$ plane for noise corrected event data	94

LIST OF TABLES

Table		Page
1.	Location and Yield Data for Pahute Mesa Events.	11
2.	Material Properties Data for Pahute Mesa Events.	12
3.	Source-Surface Travel Time Data	13
4.	Conventional m_b for HNME Recordings	21
5.	$\hat{m}_b$ for HNME Seismograms	39
6.	Source Region Crustal Structure for Synthetic Seismogram Calculations	42
7.	Receiver Region Crustal Model	43
8.	Instrument Response for the KS 36000 Seismometer	45
9.	Parameters for the P-pP Lag Time in the Synthetic Seismogram Calculations	50
10.	Parameters for the P_s Phase in the Synthetic Seismogram Calculations	51
11.	Summary of m_b and $\hat{m}_b$ Data	57
12.	Amplitudes and Periods of the Seismograms of Figure 24.	81

I. INTRODUCTION AND SUMMARY

1.1 BACKGROUND

The objective of the Systems, Science and Software (S^3) research program is to extend our present understanding of the excitation of seismic waves by underground explosions and earthquakes. Toward this objective, we are conducting theoretical and empirical studies of ground motions from the two classes of sources. In particular, our efforts are directed toward the development of improved methods for discriminating between the seismic signals from earthquakes and explosions and the development of improved methods for estimating explosion yield.

This report summarizes the work done during the first three-month period of the contract.

1.2 SUMMARY OF RESEARCH DURING THIS QUARTER

Our work during this quarter has included research in a number of areas. Research projects are briefly summarized below.

Source Calculations

A. Explosion Source Modeling

Spherically symmetric one-dimensional calculations for the SALMON event in the Tatum salt dome in Louisiana have been reported earlier. These calculations, based on laboratory material properties for salt, gave a reduced displacement potential (RDP) approximately a factor of two lower than the RDP based on measured acceleration and velocity data. In the present reporting period, we have been proceeding with a program aimed at resolving the discrepancies between our calculations and the data.

An axisymmetric two-dimensional calculation in which the material is initially assumed to be in uniaxial strain (including a shear stress) has been completed. This prestress condition gives an asymmetric radiation pattern, with a 30 percent increase in static displacement at measuring stations at shot level, but a 60 percent decrease vertically. Further investigation has linked this radiation pattern directly to the in situ shear stress. Another two-dimensional calculation has been completed which included the anhydrite, limestone, and sediments above the working point. We concluded that these layers could not significantly increase the horizontal static displacement at shot level.

An intensive literature review of the material properties of salt rocks is near completion. We have found extensive in situ and laboratory data for salt rocks, much of it developed in connection with the Waste Isolation Pilot Plant (WIPP). Based on this data, we have introduced thermal softening into our salt constitutive model. Calculations have been made using thermal softening plus a more judicious choice of elastic constants based on in situ seismic data, and a failure surface which envelopes the great mass of laboratory salt data. The latest one-dimensional calculation gives an RDP only 20 percent lower than the measured data and peak stresses and velocities, well within the scatter of the measurements. Thus, it appears that the strain rate dependent constitutive behavior of salt should be included in our model.

B. Earthquake Modeling on the ILLIAC IV Computer

This work is summarized in Section 1.6 and described in detail in Section V.

Discrimination

This work is summarized in Section 1.7 and described in detail in Section VI.

Yield Determination

A. Time Domain m_b

Some procedures for improving the accuracy and convenience of the measurement of time domain m_b are proposed in summary form in Section 1.3. A detailed discussion is given in Section II.

B. $\hat{m}_b$ An Automated Spectral Magnitude

A new body wave magnitude, m_b, is proposed in Section III. This section is summarized in Section 1.4.

C. $\hat{m}_b$ for Synthetic Seismograms

This work is summarized in Section 1.5 and is described in detail in Section IV.

Small-Scale Experiments

We have now successfully test fired two of the miniature spherical charges for use in the model experiments. The first spheres constructed would not detonate because of impurities in the explosive, PETN; this problem has now been corrected. A repeatable set of construction procedures is being developed. The detailed design of the initial proof experiment has been started; the objective of this experiment will be duplication of the results obtained in the 1977 tests.

Selected Geological Studies

A meeting of the Russian Geophysics Study Group was held at SDAC on December 11 and 12. The group included representatives of: (1) government agencies who are funding seismic discrimination research (ARPA, AFTAC, CIA), (2) contractors who are carrying out research in seismic discrimination (S^3, Teledyne-Geotech), (3) groups that are monitoring the Russian earth science literature (USGS, RAND, LLL), and

(4) geophysical consultants who are knowledgeable about the Russian earth science research in their areas of expertise (Alan Ryall, Shelton Alexander, Rob Wesson, George Keller, George Woolard, Alex Malahoff). The general objective of the meeting was to assess the adequacy of the existing geophysical data base to be used in seismic calculations for potential Russian testing areas. The opening session centered on a series of presentations by the contractors in which they attempted to provide quantitative estimates of the sensitivity of the calculations to uncertainties in the specification of the geophysical parameters of the source region and propagation paths. This was followed by a series of presentations by groups that are monitoring the Russian earth science research in which an attempt was made to summarize the status of various efforts to define values for the physical parameters of interest. This was followed by an open discussion in which gaps in the existing data base were identified and possible means of filling these gaps were suggested by the various consultants. Minutes of the meeting are currently in preparation and should be available for distribution in the coming month.

Magnitude-Yield Improvements

Initial contact has been made with AFTAC and sample ground motion spectra have been obtained. A quantitative description of the data and a list of the events and stations for which data are available is now being compiled.

Ground Motion Analysis

A systematic search for all published free-field seismic data for events in tuff, rhyolite and alluvium is underway.

1.3 SUMMARY OF SECTION II: "SEISMIC WAVEFORMS AND TIME DOMAIN m_b"

Body wave magnitude, m_b, is an important single parameter used to describe a large body of data, seismograms from many stations. Conventional m_b is based on direct measurements made by an analyst from analog playouts of the data and includes a correction for the response of the seismometer at the apparent period of the phase measured. When digital data are available, as is increasingly the case, this procedure is unnecessarily cumbersome and prone to error.

We suggest a semi-automated procedure that essentially eliminates measurement errors. We first filter all seismograms so they appear as if recorded by the same seismometer. This removes a source of systematic differences that can be 0.2 m_b units or more. The time and amplitude of peaks on the record are then determined automatically by a parabolic fit to a moving three point window. The phase to be used for m_b is selected by direct examination of the waveform and its period and amplitude are read from a table.

The semi-automated procedure outlined above is demonstrated by applications to HNME recordings of eleven Pahute Mesa explosions. The resulting m_b are compared to those given by SDAC. A more complete description of this work is given by Bache (1979).

1.4 SUMMARY OF SECTION III: "$\hat{m}_b$, AN AUTOMATED SPECTRAL MAGNITUDE"

In this section our objective is to determine and test an automated spectral magnitude which we call $\hat{m}_b$. This magnitude is based on the spectral amplitude in a narrow window in both time and frequency. The concept of the $\hat{m}_b$ has emerged from parallel development of an automated algorithm for nuclear explosion detection and discrimination. The basic procedure

on which we base the detection, discrimination and $\hat{m}_b$ determination is the same and is contained in the MARS (Multiple Arrival Recognition System) program.

Like any magnitude measure, the $\hat{m}_b$ is an empirical measure that must be developed by testing on actual data. The data set used in Section III includes HNME recordings of eleven events. We describe the application of MARS to these data in considerable detail and show how the $\hat{m}_b$ is computed. The basic operation is filtering with a Gaussion filter that is narrow in both time and frequency. Empirical tests lead to a preferred filter which has a width of 0.16 Hz or 4 seconds. Here the width is defined to include the central region that contains 68 percent of the area under the Gaussion filter.

Bache (1979) discussed the $\hat{m}_b$ for a much larger data sample including seismograms from six stations. He concludes that $\hat{m}_b$ is at least as good a magnitude measure as the most carefully determined time domain m_b, at least for high signal/noise data.

1.5 SUMMARY OF SECTION IV: "$\hat{m}_b$ FOR SYNTHETIC SEISMOGRAMS"

To improve understanding of the $\hat{m}_b$, we apply it to synthetic seismograms that closely match the HNME recordings of three Pahute Mesa explosions. The construction of these synthetic seismograms has considerable intrinsic interest and this is described.

1.6 SUMMARY OF SECTION V: "THREE-DIMENSIONAL EARTHQUAKE MODELING"

In Section V, we summarize our earthquake source modeling research using the ILLIAC computer. Much of this work was accomplished under a separate contract with Air Force Geophysics Laboratory and is reported in detail by Day, et al., (1978). The results presented in this section are a summary of those

given in our report to AFGL. We also discuss our plans for research with this model under this contract.

Two three-dimensional finite difference calculations were performed for faults with constant rupture velocity in a uniform prestress field. In one case, the medium was modeled as perfectly elastic; in the second case, the medium was elastic-plastic. Accuracy of the numerical method has been verified by comparison to an exact, closed-form solution. Near- and far-field seismic signals have been obtained from the numerical solutions. Comparing the radiated field for the finite difference solution to that for the source model of Archambeau has helped clarify the physical interpretation of the parameters of the Archambeau spherical source model.

The inclusion of plastic yielding in the second finite difference calculation is a significant step toward incorporating realistic rock mechanics into the fault model. It was found, however, that this simple form of plasticity did not reduce the large velocity peaks observed on the fault plane in the elastic case. This result supports previous studies which have suggested that an abrupt stress drop is inconsistent with bounded velocities.

1.7 SUMMARY OF SECTION VI: "DISCRIMINATION EXPERIMENT"

Two modifications were made to the MARS program that we are using in the discrimination experiment. One of these involved the development of an algorithm for estimating and correcting for the effects of local seismic noise (i.e., either background noise or signal coda) on a transient signal. The second modification consists of averaging weighted magnitude estimates at several different frequencies over a high and low frequency band. The weights are based on the ratio of signal power to noise power.

Event seismograms were processed with the modified MARS program for classified stations. Preliminary results

based on 52 events recorded at one or more of these stations indicate that the variable frequency magnitude (VFM) approach can successfully discriminate events down to small magnitude levels at stations with low background noise levels. There is also an indication that stations located over high-Q upper mantle regions (e.g., shields) provide better separation of earthquakes and explosions that stations located in tectonic regions of high heat flow and large positive (slow) travel-time residuals (by inference, low-Q upper mantle). This tentative result will be examined in more detail when the total data base (classified and unclassified stations) is completed.

II. SEISMIC WAVEFORMS AND TIME DOMAIN m_b

2.1 INTRODUCTION

In this section we present a method for determining time domain m_b which uses conventional formulas, but takes advantage of the availability of digital data to reduce measurement errors. The method will be applied to recordings of Pahute Mesa explosions. The resulting m_b are, we believe, the best time domain values possible for each record. We will compare these m_b to those given by SDAC for the same records. In later sections we will be discussing a spectral magnitude called $\hat{m}_b$. These measurement error free m_b are needed for comparison to the $\hat{m}_b$.

The data to be analyzed are short period recordings of eleven Pahute Mesa events from the SDAC station HNME. The event locations are shown in Figure 1 on a plot which includes the outline of the Silent Canyon Caldera (Orkild, et al., 1969). Only STILTON lies outside the Caldera boundary.

Source information for the eleven events is summarized in Tables 1-3. The date, location and depth are given in Table 1. In Table 2 we summarize the known elastic properties of the source material and the overburden. In Table 3 are three estimates of the source-to-surface travel time which is roughly half the delay time between the teleseismic P and pP. One estimate is the quotient of the depth and the sonic velocity of the overburden. For the second estimate we use the mean overburden velocity ($\bar{\alpha}_{OVB}$) for the eleven events rather than the specific value for each event. The third estimate, the "observed", is based on the measured arrival time on the accelerogram at surface ground zero. The references for the accelerogram records are the L^3, LASL or Sandia memoranda indicated in the tables.

We will be concerned with the conventional magnitude, m_b, for these events. For each recording this is determined according to

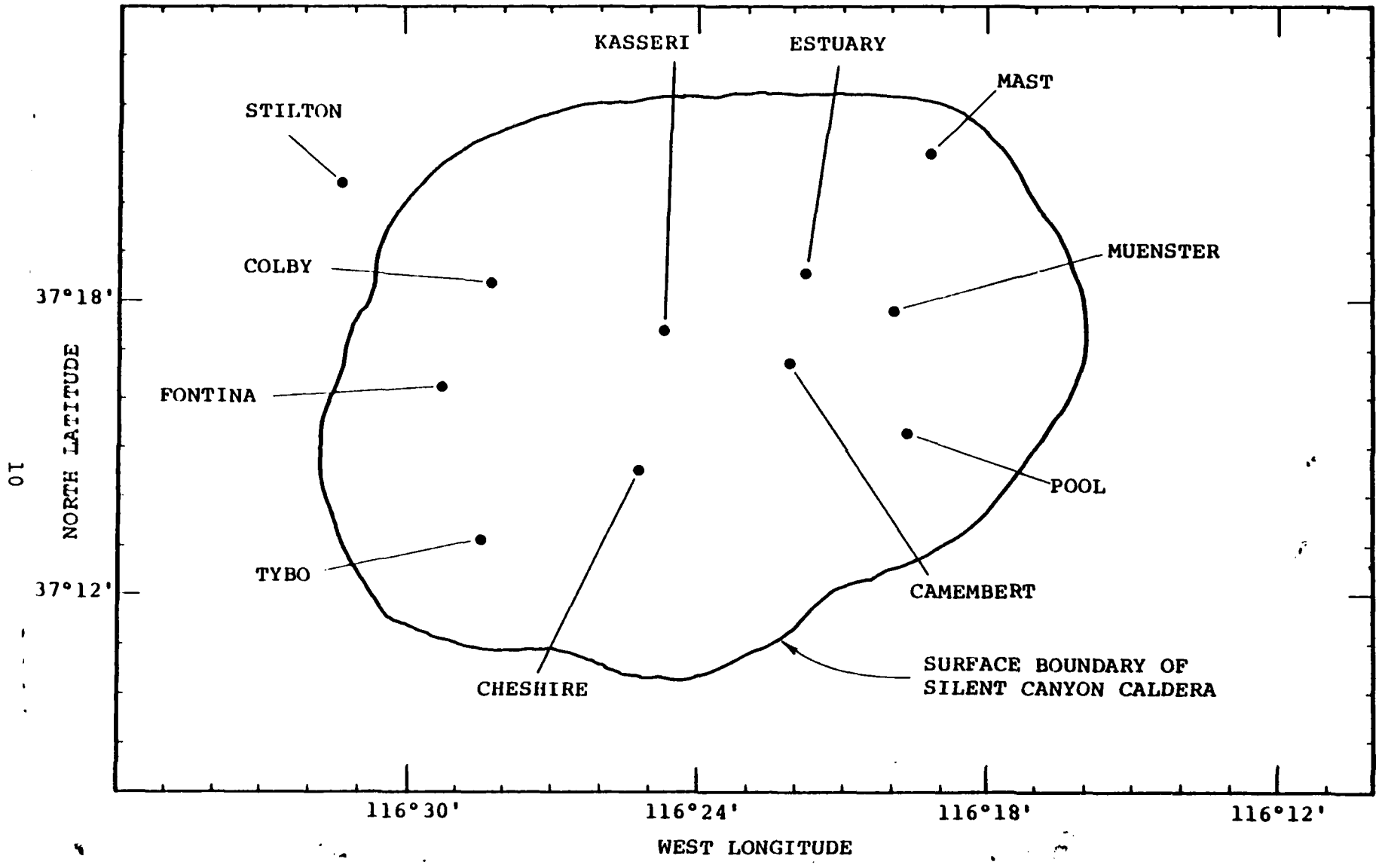

Figure 1. Locations of eleven Pahute Mesa events.

TABLE 1

LOCATION AND YIELD DATA FOR PAHUTE MESA EVENTS

Event	Date	Hole Name	Depth (m)
STILTON	3 June 1975	20P	732
POOL	17 March 1976	19P	879
ESTUARY	9 March 1976	19G	869
TYBO	14 May 1975	20Y	765
MAST	19 June 1975	19U	911
CHESHIRE	14 February 1976	20N	1167
CAMEMBERT	26 June 1975	19Q	1311
MUENSTER	3 January 1976	19E	1452
COLBY	14 March 1976	20AA	1273
KASSERI	28 October 1975	20Z	1265
FONTINA	12 February 1976	20F	1219

TABLE 2

MATERIAL PROPERTIES DATA FOR PAHUTE MESA EVENTS

Event	Material	Source Medium α (km/sec)	Source Medium ρ (gm/cm^3)	Overburden α_{OVB} (km/sec)	Overburden ρ_{OVB} (gm/cm^3)
STILTON	Rhyolite	2.62	2.30	2.15	1.80
POOL	Tuff	3.47	2.18	2.87	1.96
ESTUARY	Rhyolite	3.30	2.14	2.66	1.98
TYBO	Tuff	3.63	2.10	2.28	2.00
MAST	Rhyolite	4.20	2.45	3.88	2.24
CHESHIRE	Rhyolite	3.78	2.40	3.21	2.10
CAMEMBERT	Tuff	3.35	2.20	2.90	2.10
MUENSTER	Tuff	3.03	2.30	2.90	1.98
COLBY	Tuff	2.84	1.90	2.79	1.90
KASSERI	Tuff	3.11	2.20	3.04	2.00
FORTINA	Tuff	3.31	2.00	2.86	2.00
Mean $\pm$ Standard Deviation		3.33 $\pm$ .44	2.20 $\pm$ .16	2.87 $\pm$ .46	2.01 $\pm$ .11

TABLE 3

SOURCE-SURFACE TRAVEL TIME DATA

Event	Depth/α_{OVB}	Depth/$\bar{\alpha}_{OVB}$	Observed	Reference Memorandum*
STILTON	0.34	0.26	-	-
POOL	0.31	0.31	0.37	R. S. Fitzhugh, LASL, 4-9-76
ESTUARY	0.33	0.30	0.39	R. S. Fitzhugh, LASL, 4-2-76
TYBO	0.34	0.27	0.32	W. Wheeler/R. Preston, LLL, 3-1-76
MAST	0.23	0.32	0.36	R. S. Fitzhugh, LASL, 7-17-75
CHESHIRE	0.36	0.42	0.52	J. W. Long, Sandia, 4-7-76
CAMEMBERT	0.45	0.46	0.45	J. W. Long, Sandia, 10-30-75
MUENSTER	0.49	0.51	0.52	J. W. Long, Sandia, 2-9-76
COLBY	0.46	0.44	0.45	J. W. Long, Sandia, Personal Communication
KASSERI	0.42	0.44	0.44	J. W. Long, Sandia, 12-31-75
FONTINA	0.43	0.42	-	-

*Provided by T. A. Weaver, LASL

$$m_b = \log \frac{A}{T} + B(\Delta) \qquad (1)$$

where A and T are the amplitude and period for a particular phase on the seismogram with A corrected for the instrument amplification at the period T. The $B(\Delta)$ is the standard Gutenberg-Richter distance correction which is 3.23 for the NTS-HNME range of 36.7 degrees. We will make no correction for distance variations between events since these are less than $\pm$ 0.01 m_b units in most cases. The S_c represents source-path-station corrections which may be determined empirically and included. However, we will take S_c to be zero in this case.

The instrument amplification can be an important factor in the m_b formula. These eleven events were recorded by two different seismometers. The 1975 events were recorded by the 18300 while the KS36000 was operating for the others. The amplification curves for these two seismometers are plotted in Figure 2. The KS36000 amplitude response was provided tc S^3 in a 13 March 1978 memorandum by Captain M. J. Shore, VSC. The phase response was obtained by assuming the instrument was a minimum phase system. The amplitude and phase are then related through Hilbert transforms. The scheme for computing the phase response from the amplitude response is that of Bolduc, et al. (1972). For the 18300, amplitude and phase response data for HNME were provided in a letter by R. W. Alewine, VSC. The Hilbert transform program was used to recompute the phase which turned out to be a smoothed version of the given data. The HNME station logs were checked against the nominal 18300 and KS36000 curves and were found to be in good agreement for all eleven events.

In the remainder of this section we will present the waveforms as they were given to us and list the m_b given by the SDAC event reports. These values will be compared to

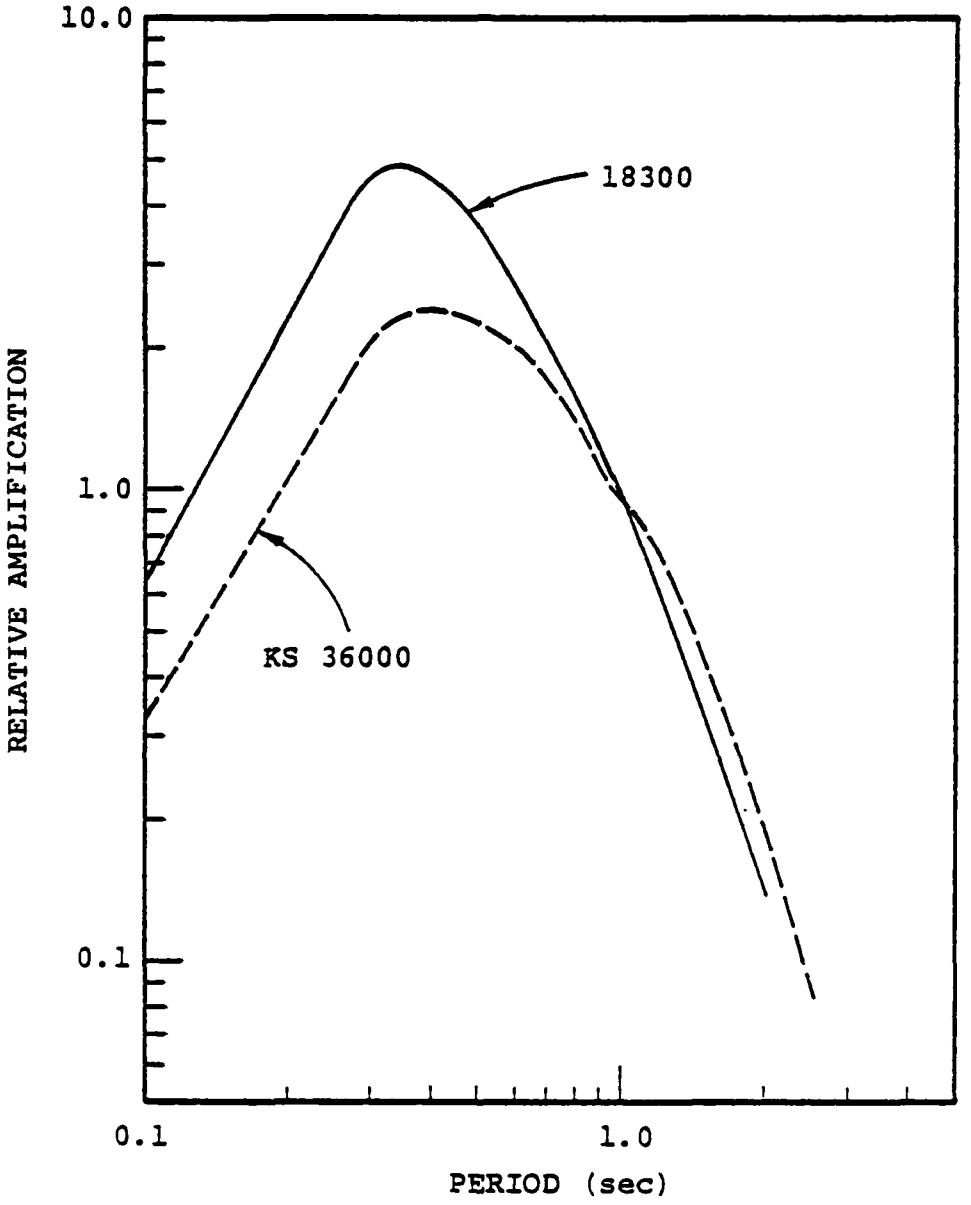

Figure 2. Relative amplitude response for two instruments used at the HNME site.

time domain m_b computed by us using Eq. (1), but with a new method for determining A and T. We call this a semi-automated time domain m_b.

2.2 A SEMI-AUTOMATED TIME DOMAIN m_b

To compute m_b from Eq. (1) we need to measure A and T and this is usually done by hand from analog playouts of the data. The most important errors inherent in this procedure may be divided into two categories:

- It is difficult to measure the period with an error much less than 0.1 to 0.2 seconds. The instrument response is rapidly changing in the 0.7 to 1.4 second range where the measurements are usually made (Figure 2). Fortunately, the approximately inverse proportionality between T and the amplification does tend to compensate for errors in T and reduce their effect in many cases.
- Even if we could measure the period precisely, the signal is not monochromatic. Thus, correcting to true ground motion by dividing by the instrument amplification at the period T must introduce error. For a given waveform the error is constant, so for similar signals recorded by identical instruments, the main effect is a baseline shift. However, the error is compounded when data from instruments with different response curves are mixed.

We wanted to compute time domain m_b values with the errors minimized to the extent possible. This has, of course, a considerable amount of inherent interest. Our original motivation was, however, to remove as many obscuring effects as we could for comparison of time domain m_b with our new $\hat{m}_b$. Also, as long as digital data were available, we could see little point in making measurements from analog playouts.

Our semi-automated time domain m_b involves two steps which may or may not be used together. First, we use the computer to make the measurements. The data are passed through a sliding three-point window. Whenever the center point is greater than or less than both end points, the three points are fit by a parabola. The time and amplitude of the peak are saved. The period, T, is computed from the time difference between adjacent peaks. Using the apparent instrument response, log (A/T) is then computed for each cycle on the record. To obtain an m_b, the analyst need only inspect the waveform to select a phase and then read log A/T from a printed table. This algorithm is contained in a subroutine called PFIT which is routinely applied to synthetic or observed data for which m_b or M_s information is desired.

We have outlined a method to make time domain measurements convenient and accurate when digital data are available. What about the correction for instrument response? We believe the effect of this correction is most consistent when all recordings are prefiltered to appear as if recorded by the same instrument. That is, we Fourier transform the signal, multiply by the quotient of the actual and standard responses and inverse transform. The new recordings can then be processed by PFIT. In later sections we will show that changing the seismograms to a standard instrument can remove a significant source of error which is far from normally distributed.

2.3 HNME DATA

The HNME seismograms are shown in Figure 3 as they were recorded. They are arranged on the page in order of increasing depth as given in Table 1. As noted in Section 2.1, these seismograms were recorded with two different instruments. The main difference between the two (Figure 2) is at short periods where the 18300 is significantly larger.

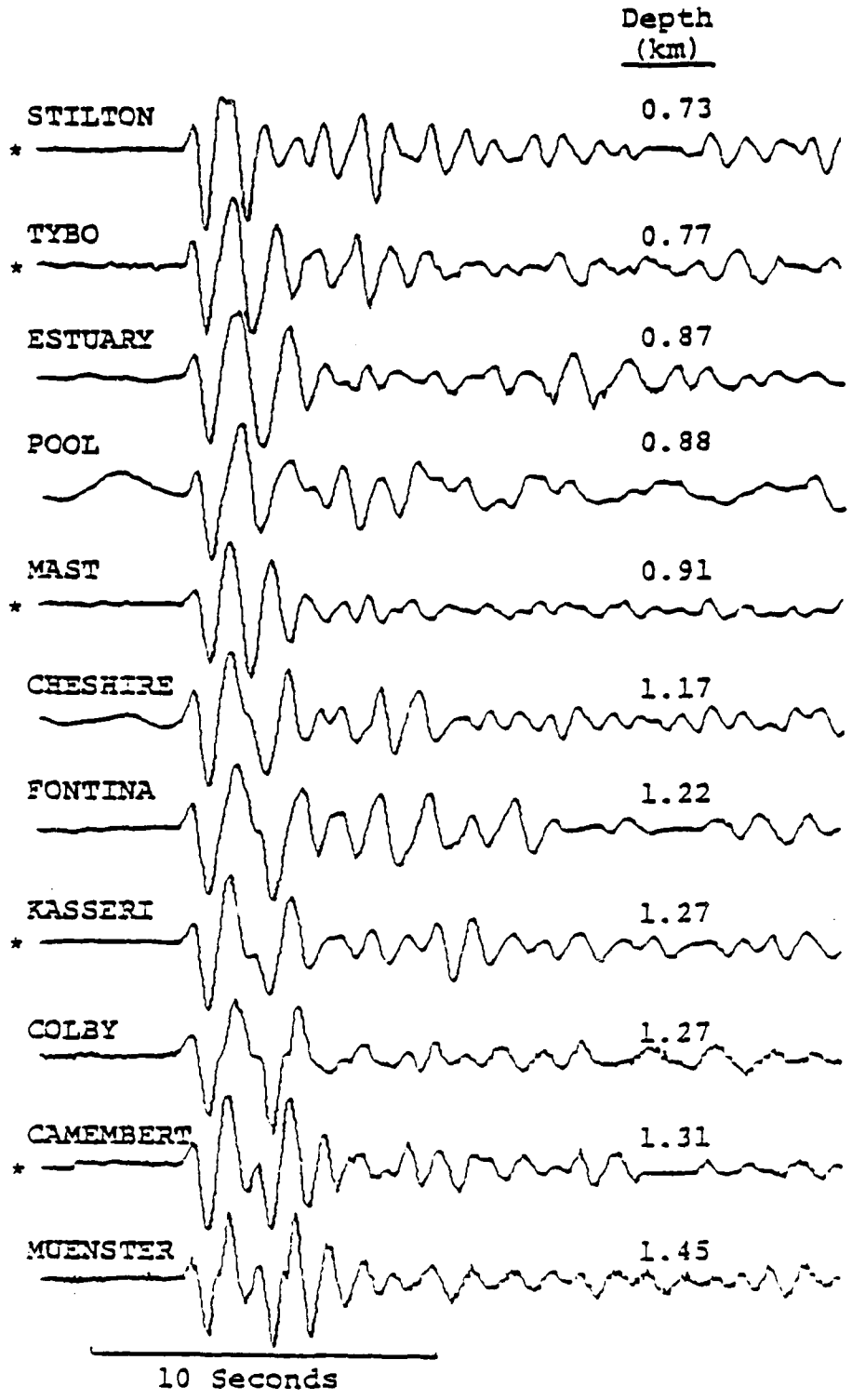

Figure 3. The HNME recordings of eleven Pahute Mesa events are arranged according to increasing depth. The asterisk denotes events recorded by the 18300 seismometer.

In Figure 4 we replot the seismograms arranged according to increasing source-surface travel time, as given in Table 3. For all but STILTON and FONTINA, the travel-time estimate is based on the arrival time at surface ground zero. The mean velocity of the overburden (α_{OVB}) was used to estimate the time for the other two events.

In Figure 4 the seismograms recorded by the 18300 instrument were filtered so they appear as if they were recorded by a KS36000 seismometer. The effect is to remove some of the high frequency details from the 18300 recorded events (compare to Figure 3).

Displayed as in Figure 4, record characteristics related to the source-surface travel time become apparent. The nature and causes of these differences are subjects for a separate study. It is clear that the first few cycles of the seismograms contain at least three distinct arrivals. First, there is the direct P wave. This is followed a second or so later by an arrival we would identify as pP. A break in the waveform associated with this arrival can be seen on the MUENSTER, COLBY, ESTUARY and STILTON records, but it is less clear on the others. The third arrival is very distinct and has a clearly apparent depth moveout. It arrives about two seconds after P, too late to be pP. Other authors have noted the presence of a secondary phase like this on similar explosion records and have associated it with spall closure (e.g., Springer (1974)). Following Springer, we will denote this phase by P_s.

In Table 4 we list two estimates for m_b for the KS36000 recorded events and three estimates for the other five events. The SDAC data are taken directly from the SDAC event reports.

The S^3 m_b measurements were made using the procedure described in the preceding section. The PFIT routine was

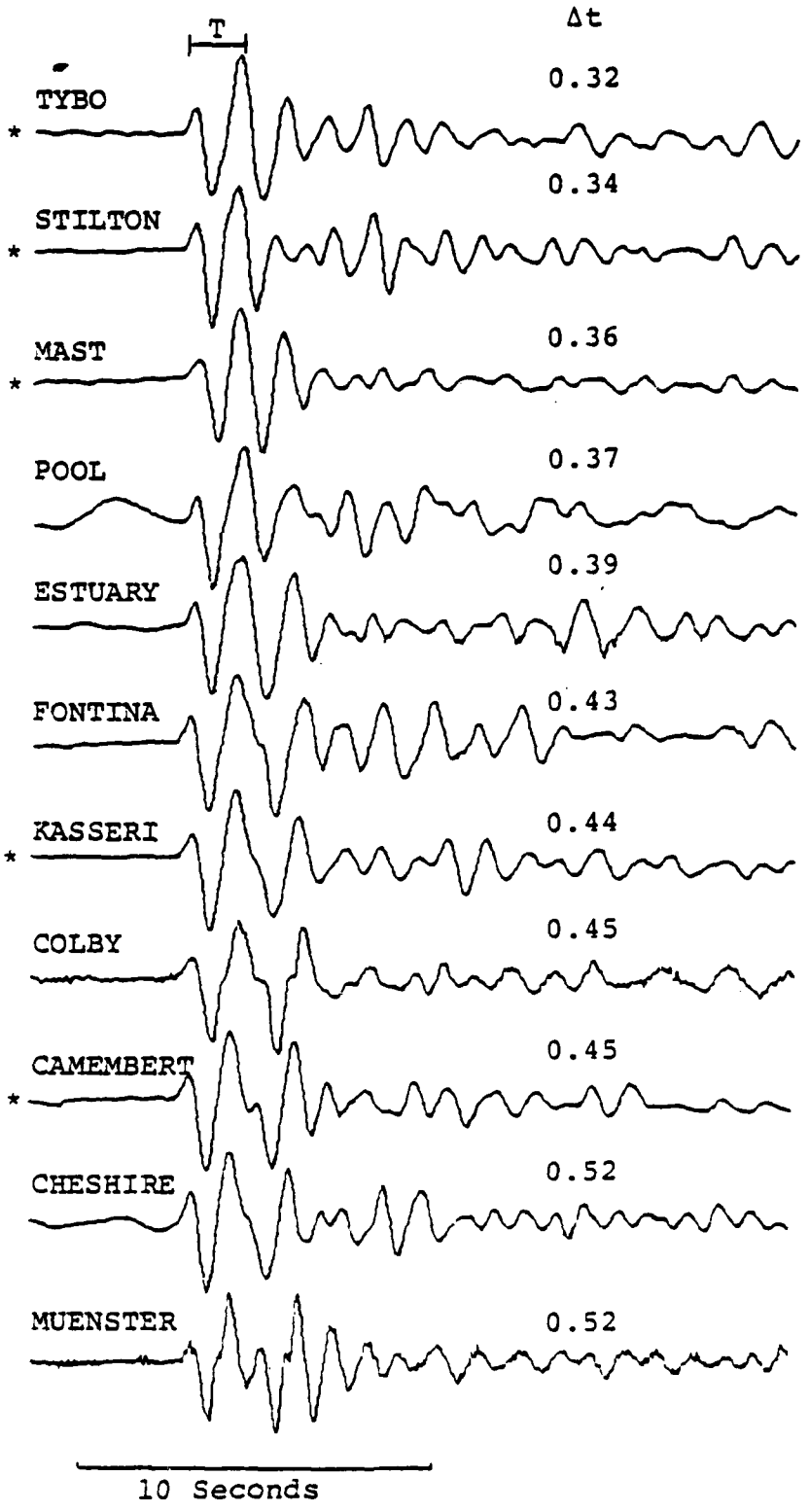

Figure 4. The HNME recordings are arranged according to increasing source-surface travel time (Δt from Table 3). All 18300 recorded events (marked with an asterisk) have been filtered to appear as if recorded by the KS36000 instrument.

TABLE 4

CONVENTIONAL m_b for HNME RECORDINGS*

	SDAC** Data		S^3 Measurements 18300		KS36000	
Event	m_b	Period	m_b	Period	m_b	Period
STILTON	5.55	0.7	5.60	0.8	5.86	1.1
POOL	6.37	1.3			6.29	1.3
ESTUARY	6.25	1.5			6.07	1.3
TYBO	5.37	1.4	6.20	1.2	6.26	1.2
MAST	6.21	1.1	6.10	1.0	6.25	1.1
CHESHIRE	6.03	1.0			6.02	1.1
CAMEMBERT	6.25	1.0	6.24	1.0	6.37	1.1
MUENSTER	6.39	0.8			6.49	0.9
COLBY	6.38	0.9			6.50	1.3
KASSERI	6.46	1.0	6.50	1.1	6.59	1.2
FONTINA	6.48	1.3			6.43	1.3

*All period measurements were made from the first peak to the second peak as shown above the TYBO record in Figure 4. The amplitudes were measured from first trough to first peak.

**From SDAC event reports -- authors: J. R. Woolson, K. J. Hill, D. D. Solari, M. S. Dawkins, M. D. Gillespie, R. R. Baumstark, R. J. Markle, D. J. Reinbold.

applied to the records as they were recorded (Figure 3) and after filtering so all include the KS36000 response. For the five events with m_b from both instruments, the differences are striking. The T from the 18300 recordings are 0.14 seconds shorter, on the average, than the T from the KS36000 records. As a result, the m_b are an average of 0.14 units smaller. The differences are greatest for STILTON and the reason can easily be seen by comparing the two waveforms (Figures 3 and 4). However, the averages for the other four events are 0.10 seconds and 0.11 m_b units, still quite large.

The differences between our (mixed instrument) m_b and those given by the SDAC reports can mostly be explained by differences in the period. Our period measurements are very accurate since they were done automatically by PFIT. A major difference occurs for TYBO where the amplitude in the SDAC report must be in error. Using copies of the station logs and digital playouts of the calibration steps, we recalibrated all the data. Thus, the gain we used is probably not identical to that used by SDAC. Ignoring TYBO, the differences between the SDAC m_b and ours obtained from recalibrated data with PFIT range from -0.18 to 0.12 m_b units.

III. $\hat{m}_b$, AN AUTOMATED SPECTRAL MAGNITUDE

3.1 INTRODUCTION

In this section we describe a new magnitude measure that we call $\hat{m}_b$. This magnitude is based on the spectral amplitude in a narrow window in both time and frequency. Our intention is for the $\hat{m}_b$ to provide an estimate of the spectral energy of the direct P wave arrival. This is precisely what is needed to infer explosion yield. Empirical tests suggest that the $\hat{m}_b$ is a stable measure of signal energy and should reduce the scatter in network m_b estimates. Another important advantage is that the $\hat{m}_b$ can be computed as part of an automated seismic data analysis system.

An important problem for VSC is the development of relationships between body wave magnitude and nuclear explosion yield. Empirical work directed toward this objective has focussed on time domain m_b measured from the analog recordings (e.g., Dahlman and Israelson, 1977). The idea of replacing such time domain measures with some spectral magnitude has been around a long time. For both earthquakes and explosions the spectral energy in the direct P wave is probably the best indicator of the source energy.

There are several reasons why a spectral magnitude has not emerged to replace the conventional m_b. Foremost is probably the fact that the data must be in digital form and be conveniently accessible for analysis. There is now a large enough digital data base that this should no longer be a problem. Another reason is that a really satisfactory algorithm for computing spectral m_b has not yet emerged. However, promising results have been obtained in some recent work at the Seismological Institute, Uppsala (Shapira and Kulhánek, 1978) and at VSC (Woodward, personal communication). In the former study the log A/T in (1) is replaced by the mean of the Fourier spectrum of the signal over a narrow frequency range; the

authors suggest 0.47 to 0.78 Hz. They find that this magnitude has less scatter than conventional m_b over the five station Swedish seismograph station network. The spectral magnitude used by Woodward at VSC is similar to that of Shapira and Kulhánek and he finds less scatter in magnitude versus log yield for NTS explosions.

The spectral magnitudes mentioned in the previous paragraph are based on the Fourier spectrum of some signal window that is much broader than the P wave itself. Later arriving phases then can have a strong effect on the spectral amplitude. Knowledge of this disadvantage has probably dampened enthusiasm for magnitudes based on spectral information.

The idea for the $\hat{m}_b$ emerged from our development of the automated algorithm for nuclear explosion detection and discrimination on which the MARS (Multiple Arrival Recognition System) program is based. The MARS algorithm is based on analysis of seismic waveforms with a suite of narrow-band filters. For detection and discrimination the amplitude of the filter output is used to define a VFM (variable frequency magnitude). Our $\hat{m}_b$ is based on the VFM.

In the sequel we first describe the MARS algorithm and its application to define $\hat{m}_b$. As examples, the HNME seismograms from Section II are processed. A clearer understanding of the sensitivity of $\hat{m}_b$ to the waveform character can be obtained by processing synthetic seismograms. Some results of such an exercise are presented in Section IV.

3.2 MARS ANALYSIS AND THE DEFINITION OF VFM

The MARS program has been developed at S^3 during the past several years. The algorithm and much of the program design is due to Professor C. B. Archambeau, an S^3 consultant. The program development has been primarily by Dr. J. F. Masso.

Applications have included nuclear explosion detection and discrimination (Savino and Archambeau, 1974; Savino, et al., 1974; Savino, et al., 1975; Rodi, et al., 1978), decomposition of multiple events (Lambert, et al., 1977; Lambert and Bache, 1977) and analysis of surface wave dispersion (Bache, et al., 1978). A version of the program is currently operational on the Network Event Processor at VSC. The MARS algorithm also promises to be a powerful event detector and, in short, a tool that can form the core of a complete seismic data analysis system.

Briefly described, the MARS algorithm is as follows. The seismogram is Fourier transformed and filtered by a narrow-band, Gaussian filter. The Hilbert transform of the filtered spectrum is then constructed and inverse transformed to obtain the envelope function. The peaks of the envelope function indicate phase arrivals of energy in a narrow-band of frequencies near the filter center frequency. The arrival times are accurately preserved in the times of these peaks and the relative amplitudes of the peaks reflect the relative amplitudes of arriving pulses of energy in the frequency band. The flow of operations in the MARS program is summarized in Figure 5.

The output of the narrow-band filter processing that forms the heart of the MARS program is a table including the envelope peak amplitudes (A_k) and associated arrival times (t_g) for each center frequency (f_k). Generally there are many A_k, t_g pairs for each filter, depending on the complexity of the signal.

Let us look more closely at the narrow-band filter. As given in Figure 5, the functional form is

$$\tilde{F}^{(k)}(w) = \sqrt{\frac{\alpha}{\pi}}\, e^{-\alpha(f-f_k)^2} \qquad (5)$$

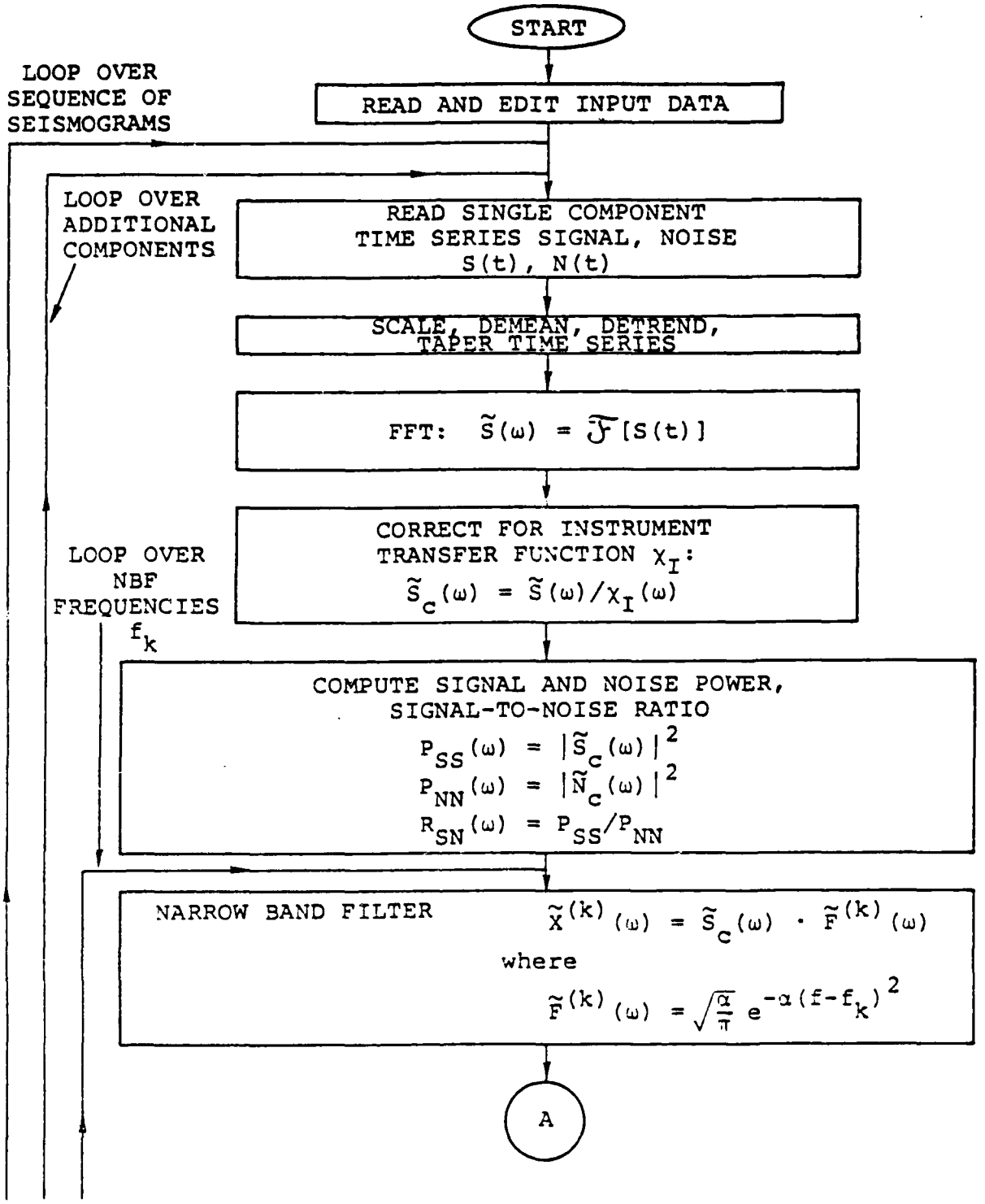

Figure 5. Schematic presentation of the MARS algorithm.

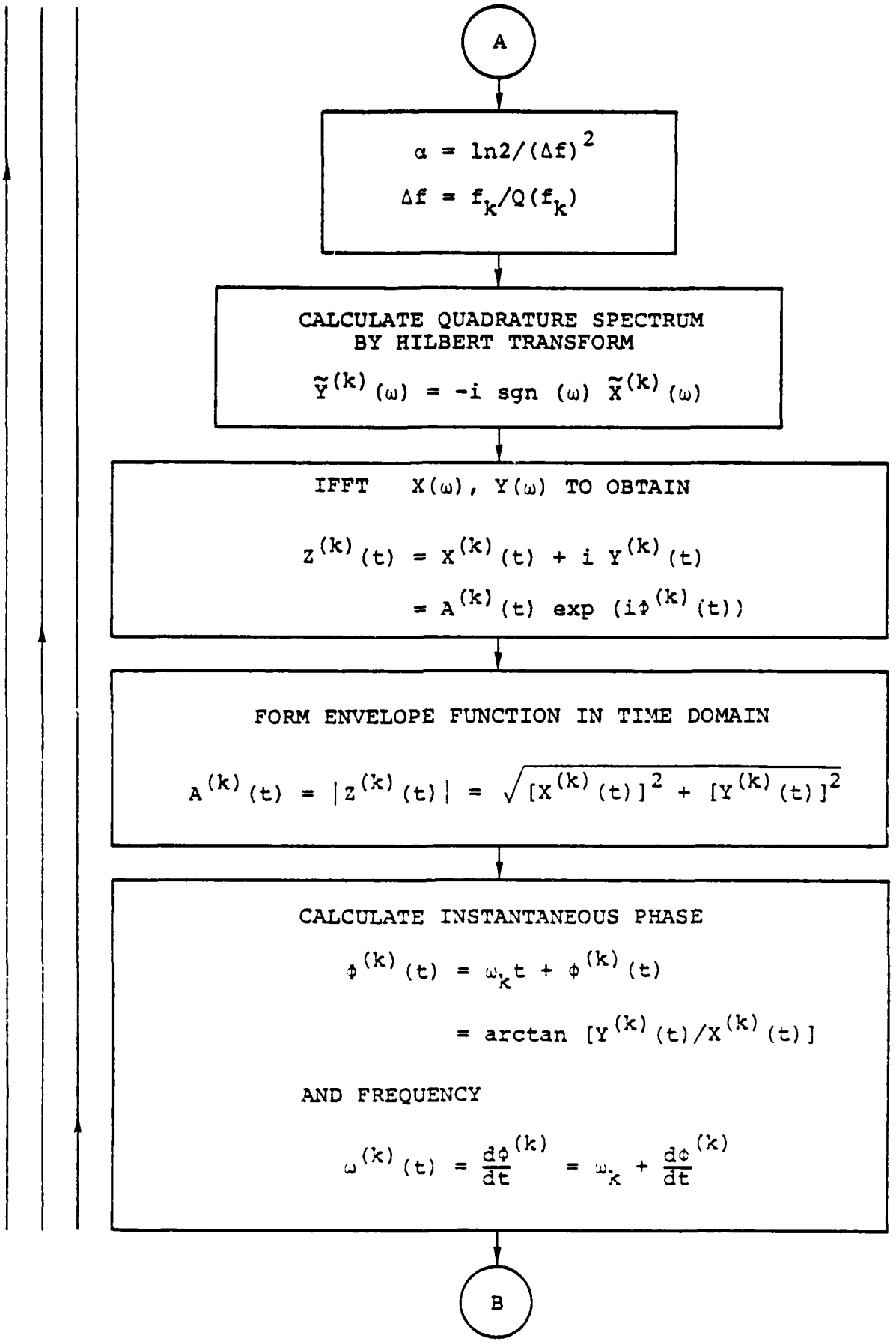

Figure 5. (continued)

where

$$\alpha = \frac{\ell n\ 2}{2} \frac{Q^2}{f_k^2} \quad .$$

Viewed as a Gaussian probability distribution, this filter has standard deviation

$$\sigma_f = \frac{1}{\sqrt{\ell n 2}} \frac{f_k}{Q} \quad , \tag{6}$$

which means that 68.3 percent of the area under the filter is contained in the frequency band $f_k - \sigma_f \leq f_k \leq f_k + \sigma_f$.

It is easily shown that the time domain expression of the filter (5) is

$$F^{(k)}(t) = \frac{2\pi}{\alpha} \cos(2\pi f_k t)\ e^{-\frac{\pi^2 t^2}{\alpha}} \quad . \tag{7}$$

The Gaussian envelope function then has standard deviation

$$\sigma_T = \frac{\sqrt{\ell n 2}}{2\pi} \frac{Q}{f_k} \quad . \tag{8}$$

We see that the width of the narrow-band filter is controlled by the parameter Q which appears in the definition of α. From (6) and (8) it is clear that the narrower the filter in frequency, the wider in time and vice versa. For high Q we get an excellent estimate of the spectral amplitude for a broad time window; there will be few A_k, t_g pairs for each filter.

For low Q the spectral estimate is less precise but the t_g are more accurate and there are generally many peaks for each filter.

A choice of a preferred Q was made by trial and error testing of different values on both synthetic and observed seismograms. For short period data sampled 20 times/second, we have adopted the following Q values:

$$\begin{aligned} Q &= 15\ f_k, \qquad f_k \geq 0.35 \quad , \\ Q &= 5.25, \qquad f_k < 0.35 \quad . \end{aligned} \tag{9}$$

The narrow band filters $\tilde{F}^{(k)}(\omega)$, for the Q values given in (9) and the f_k used in our analysis are plotted in Figure 6. For $f_k \geq 0.35$ we compute from (6) that

$$\sigma_f = 0.08 \text{ Hz} \quad .$$

Thus, the width of the filter within one standard deviation is 0.16 Hz. For $f_k < 0.35$ equation (6) gives $\sigma_f = 0.23\ f_k$ and the filter is narrower.

The corresponding time domain filters are plotted in Figure 7. From (8) we have for $f_k \geq 0.35$ that

$$\sigma_T = 1.99 \text{ seconds.}$$

The filter width is therefore about four seconds for these f_k, using standard deviation as the criterion, and somewhat wider at lower center frequencies. Clearly, this is not sufficient resolution to give distinct spectral amplitudes for phases separated by less than several seconds, even when the phases are distinguished by separate t_g. This is illustrated in Section IV where several synthetic seismograms are analyzed.

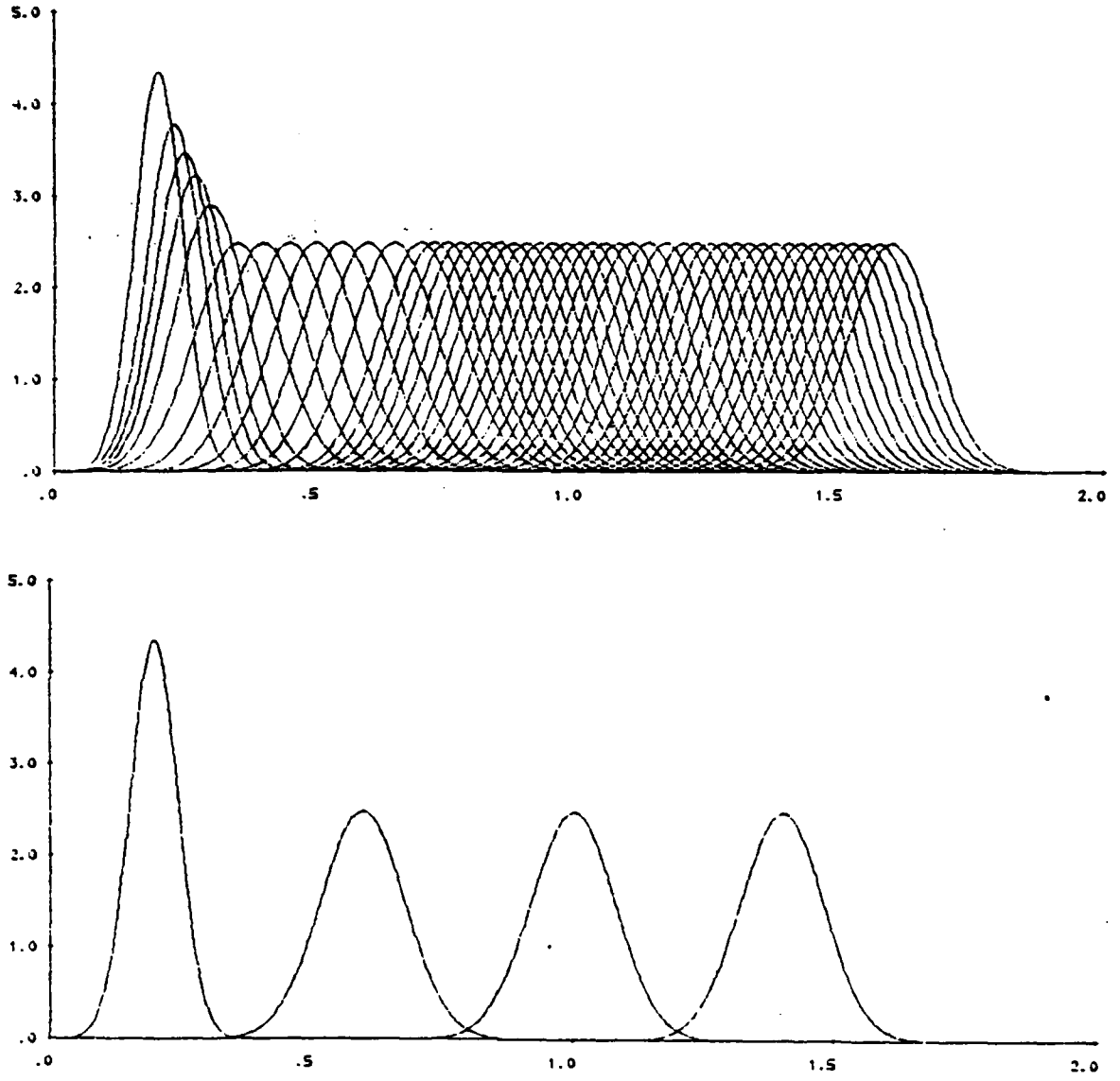

Figure 6. Forty-eight narrow band filters with center frequencies $0.2 \leq f_k \leq 1.6$ Hz are plotted versus frequency. At the bottom the filters for f_k = 0.2, 0.6, 1.0 and 1.4 Hz are plotted separately. Note that the filter shape is constant for $f_k \geq 0.35$, where Q is proportional to f_k.

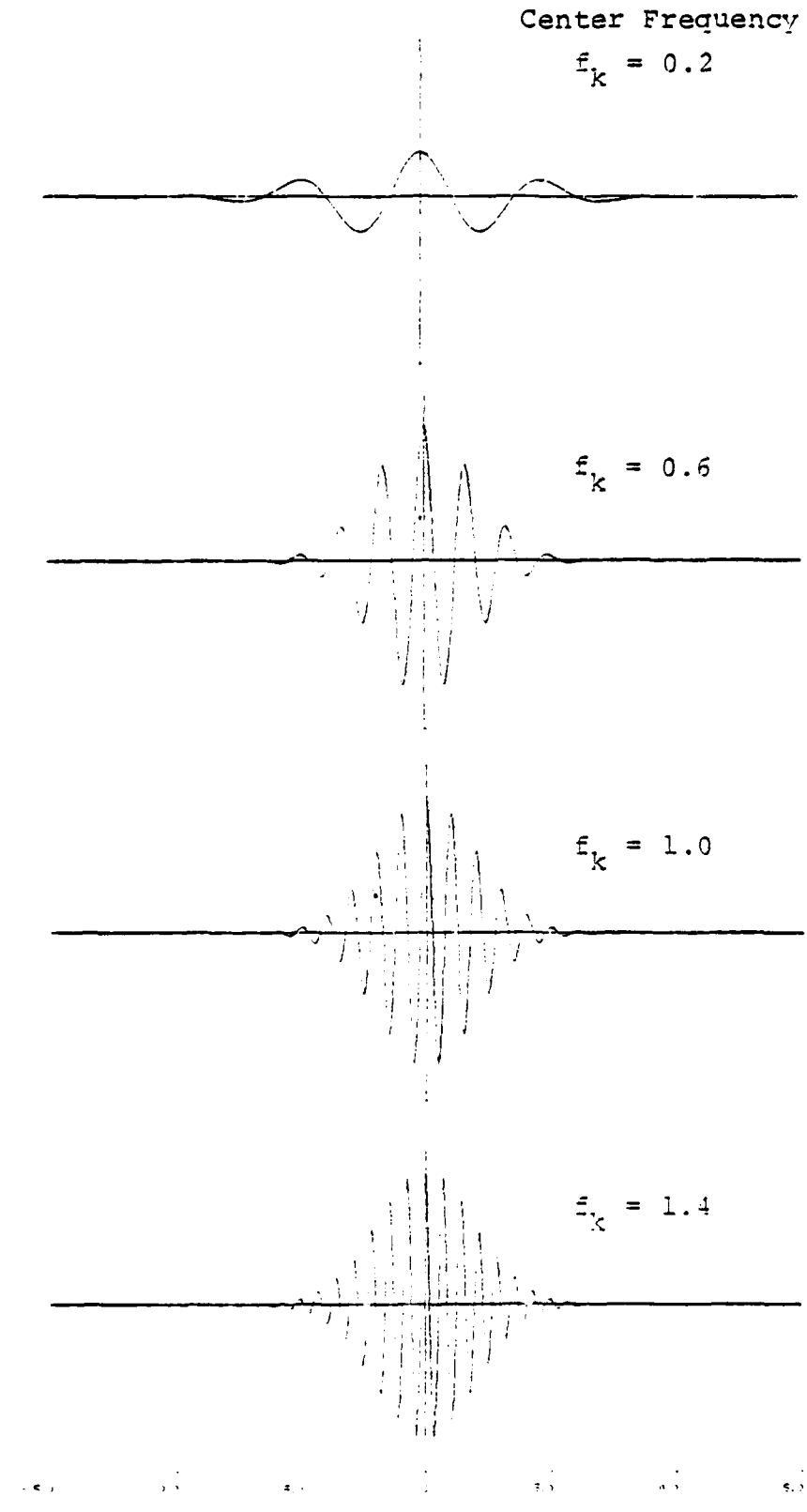

Figure 7. The time domain filters are plotted for four f_k.

The variable frequency magnitude (VFM) is denoted by $\bar{m}_b(f_k)$. For a specified envelope peak this is defined by (Savino and Archambeau, 1974; Savino et al, 1975)

$$\bar{m}_b(f_k) = \log (A_k \cdot f_k) + B_p(\Delta) \quad , \tag{10}$$

where $B_p(\Delta)$ is the usual Gutenberg-Richter distance correction for zero-to-peak amplitude. That is, $B_p(\Delta)$ is 0.3 units more than the peak-to-peak value used in (1). This formula is the frequency domain analog of the standard time domain formula for m_b, equation (1). Specification of the particular envelope peak is based on the t_g associated with that peak. That is, we choose the (narrow) portion of the wavetrain from which the $\bar{m}_b(f_k)$ is determined.

3.3 DEFINITION OF $\hat{m}_b$

The motivation for the definition of $\hat{m}_b$ is the observation that the VFM, $\bar{m}_b(f_k)$, provides an estimate of the spectral energy in a narrow band in time and frequency. The idea is to compute some average of this quantity in the region of maximum spectral energy near the P wave arrival time which is also the region sampled by conventional time domain m_b measurements.

We illustrate the $\hat{m}_b$ determination with the HNME recordings from Figure 3. These records were processed by MARS and the results are plotted in Figure 8. These plots were obtained in the following way:

- Each seismogram was Fourier transformed and the instrument response was removed from the spectrum.

- Each seismogram was filtered by forth-eight constant width narrow band filters with center frequencies (f_k) from 0.2 - 1.6 Hertz and Q specified by Equation (5).

- Envelope peak amplitudes, $A_k(f_k)$, with group arrival times, $t_g(f_k)$, within an eight second window about the P wave arrival time were selected. In many cases there are two or more such peaks.

- The largest peak for $0.35 \leq f_k \leq 1.6$ was identified. Using this peak as a starting point, one peak is then selected for each f_k, with the selection made to maximize the smoothness of t_g versus f_k and A_k versus f_k.

In Figure 8 we show log $(A_k \cdot f_k)$ and t_g versus f_k for each event. The zero crossing between the first peak and first trough is defined to be at $t_g = 0$. The amplitude quantity plotted in Figure 8 is essentially the VFM, see Equation (3).

The log $(A_k \cdot f_k)$ is a velocity-like quantity. Since the instrument response has been removed and the geometric attenuation is nearly independent of frequency, the only important filter applied to the data should be the Q operator; that is, $\exp \{ - \pi f_c t^* \}$ where t* is the travel time divided by the effective Q for the path. Thus, log $(A_k \cdot f_k)$ falls off at high and low frequency and has the peaked character seen.

The data plotted in Figure 8 are used to define $\hat{m}_b$. There are several possibilities for how this might be done. We define $\hat{m}_b$ according to

$$\hat{m}_b = \log A + B_p(\Delta) + S_c \quad , \tag{7}$$

where $B_p(\Delta)$ is the Gutenberg-Richter distance correction and S_c may be included as some empirically determined station correction. Possible definitions for A include:

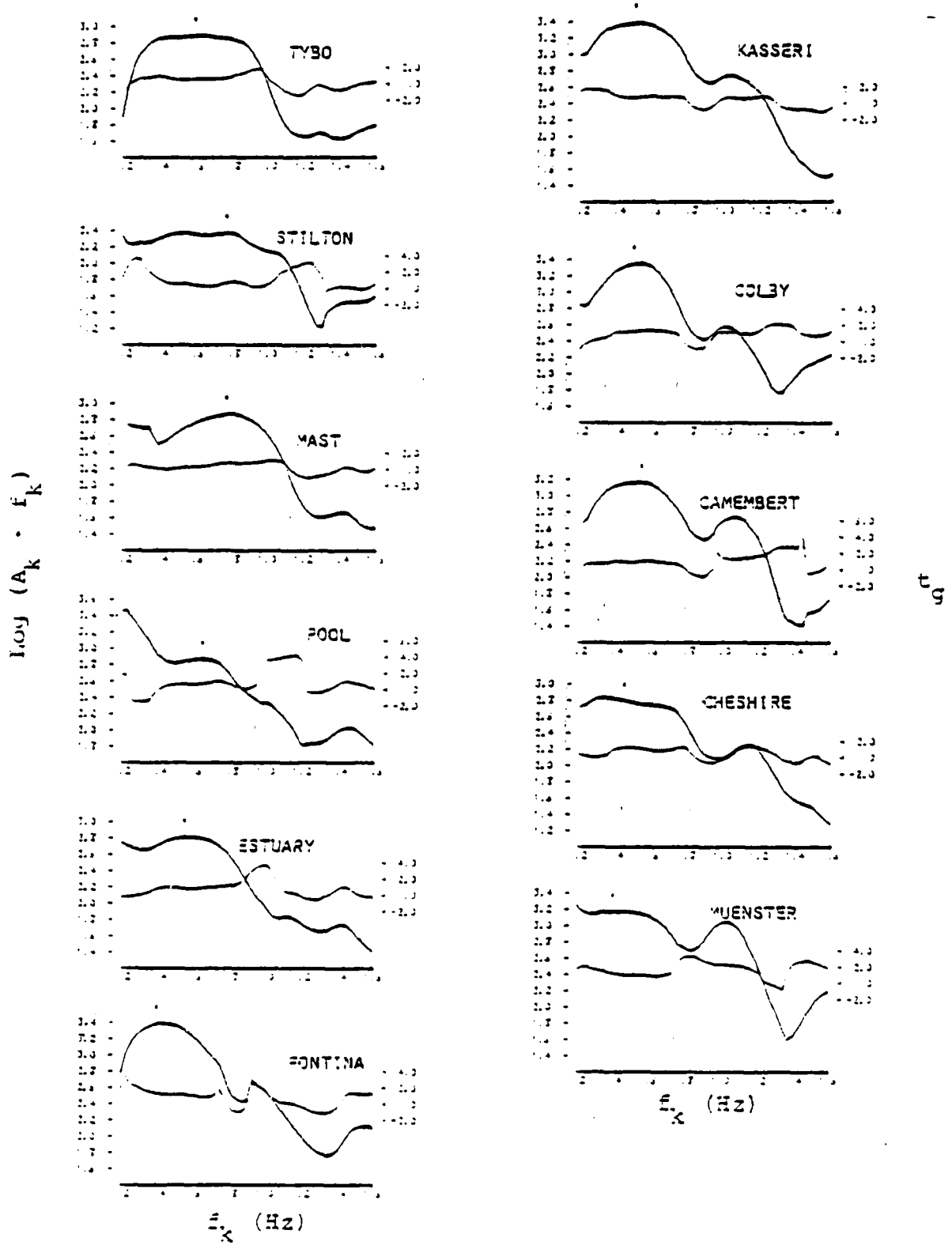

Figure 8. For each of the HNME recordings of Figure 3 we plot log $(A_k \cdot f_k)$ and t_g versus filter center frequency, f_k. The t_g scale is at the right on each plot. The band for the m_b determination is indicated by small vertical bars. The maximum log $(A_k \cdot f_k)$ in this band is marked with an asterisk.

1. A is $A_k \cdot f_k$ at a single fixed frequency;

2. A is the maximum value of $A_k \cdot f_k$ in a particular f_k band;

3. A is the average $A_k \cdot f_k$ over a fixed band;

4. A is the average value of $A_k \cdot f_k$ in an f_k band defined by requiring that t_g remain within specified limits.

These alternatives have been evaluated by testing their application to the HNME recordings of Pahute Mesa explosions described in Section II. These data lead to the conclusion that 2 and 4 are the best definitions. They seem to give equally good results. We are wary of recommending any definition based on a single frequency value and are biased toward the definition requiring some averaging over a frequency band. Thus, we prefer the t_g band-averaged A, definition 4.

In Figure 8 the maximum value of $\log (A_k \cdot f_k)$ for $f_k \geq 0.35$ is indicated with an asterisk. From this point our algorithm searches backwards and forwards in f_k to define the limits of the region within which the t_g are within one second of the t_g at the peak. The limits of this band are indicated by small vertical bars on the plots. Then A is defined by

$$A = \frac{1}{\Delta f_k} \int_{\min f_k}^{\max f_k} (A_k \cdot f_k) df \quad , \tag{8}$$

where $\Delta f_k = \max f_k - \min f_k$, with the latter two values being those indicated on the plots. The integral is evaluated by quadratures. Then $\hat{m}_b$ is computed according to (7).

The scheme we have outlined is easily automated as a post-processor of the MARS output table of A_k - t_g pairs as a function of f_k. As input we select a time window specifying the portion of the signal where we want $\hat{m}_b$ to be determined. Envelope peaks with t_g outside this window are discarded. For the seismograms analyzed in this report this window extended from three seconds before to five seconds after the first zero crossing (the t_g = 0 on the plots of Figure 8). We also specify a window for the f_k and require the limits for the integration (8) to be within that window. For this analysis no upper limit for f_k was necessary. The lower limit was usually set at f_k = 0.35 Hz. This limit was set higher in cases where the low frequency log ($A_k \cdot f_k$) seemed to be noise contaminated and we will point this out at the appropriate place.

In Figure 9 we again plot the HNME seismograms from Figure 4. A time band is indicated on each seismogram. The t_g for all A_k used in the computation of $\hat{m}_b$ fall within this band. The t_g associated with the peak log ($A_k \cdot f_k$) is marked with an asterisk.

For each t_g in the indicated band the time domain filters have the form shown in Figure 7. The portion of the signal that influences the $\hat{m}_b$ cannot be specified very precisely, but Figures 7 and 9 give a good indication of the time window that might be important. In general, this window is some 5 to 8 seconds long.

Another way to better understand the sensitivity of m_b is to apply the algorithm to synthetic seismograms. This is done in Section IV for synthetics that are nearly identical to the observed HNME recordings of MAST, CAMEMBERT, and FONTINA.

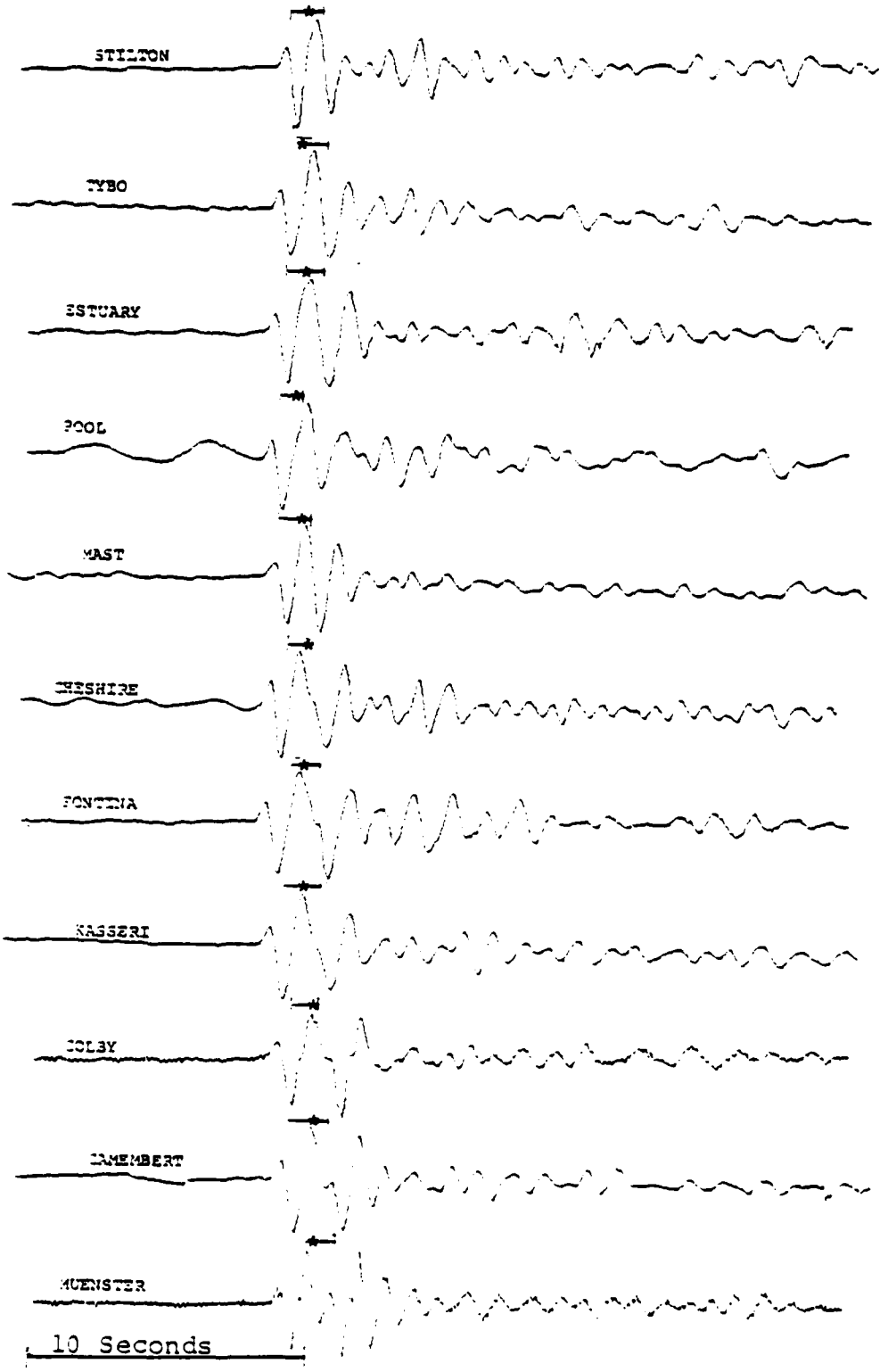

Figure 9. The HNME recordings from Figure 4 are shown with a scale indicating the limits of the t_g band used in the $\hat{m}_b$ calculation.

3.4 $\hat{m}_b$ FOR HNME SEISMOGRAMS

Using the definition given in the previous section, we compute the $\hat{m}_b$ from the data plotted in Figure 8. The results are summarized in Table 5. We give the $\hat{m}_b$ and the interval of integration for (8). This interval is also indicated by vertical bars on the event plots in Figure 8. The $\hat{m}_b$ is computed from (7) with $B_p(\Delta) = 3.53$. This is the same formula used to compute the time domain m_b listed in Table 4 and these m_b are listed. Also listed is the frequency (marked with an asterisk in Figure 8) for each event and the $\bar{m}_b$ obtained from (7) with A being the maximum log $(A_k \cdot f_k)$.

If the shape of log $(A_k \cdot f_k)$ were the same for all events, the difference between the $\bar{m}_b$ and $\hat{m}_b$ listed in Table 5 would be constant. In fact, the mean residual is 0.09 units with a standard deviation of 0.03. Thus the difference is fairly constant, though the interval of integration varies from event-to-event.

TABLE 5. $\hat{m}_b$ FOR HNME SEISMOGRAMS

Event	f_k at peak	$\bar{m}_b$ (f_k at peak)	min f_k-max f_k	$\hat{m}_b$	Table 4 m_b
Stilton	0.78	5.89	0.40-1.05	5.84	5.86
Pool	0.65	6.39	0.45-0.95	6.28	6.29
Estuary	0.55	6.34	0.35-0.88	6.25	6.07
Tybo	0.60	6.41	0.35-0.90	6.38	6.26
Mast	0.78	6.39	0.35-1.13	6.24	6.25
Cheshire	0.45	6.31	0.45-0.83	6.23	6.02
Camembert	0.55	6.69	0.35-0.80	6.60	6.37
Muenster	0.40	6.70	0.35-0.75	6.63	6.49
Colby	0.50	6.88	0.35-0.75	6.78	6.50
Kasseri	0.50	6.90	0.35-0.80	6.83	6.59
Fontina	0.40	6.91	0.35-0.75	6.79	6.43

IV. $\hat{m}_b$ FOR SYNTHETIC SEISMOGRAMS

Considerable insight into the behavior of the MARS filters and their use to define $\hat{m}_b$ can be gained by studying synthetic seismograms. In this section we first construct synthetic seismograms at the LRSM station HNME for three Pahute Mesa events, MAST, CAMEMBERT and FONTINA. We then process these synthetic records with the $\hat{m}_b$ algorithm.

The synthetic seismograms are constructed in the following way:

- The computational method is that described by Bache and Harkrider (1976).

- The explosion source function is a reduced displacement potential ($\Psi(t)$) computed with the Mueller/Murphy theory (Mueller and Murphy, 1971). The amplitude of the transformed $\dot{\Psi}(t)$ is shown in Figure 10 for the three events. The depth at which the source function was computed is indicated on the figure.

- The crustal models for the source region are tabulated in Table 6. Information used to construct these models included well-log data, average overburden velocity data and Basin and Range crustal structure information from refraction profiles (Hill and Pakiser, 1967). Some adjustments to the velocity of layers above the source were also made to change the P-pP delay time to improve the agreement of synthetic and observed records.

- For the crust in the receiver region we used the model tabulated in Table 7. The upper mantle model is HNME (Helmberger and Wiggins, 1971).

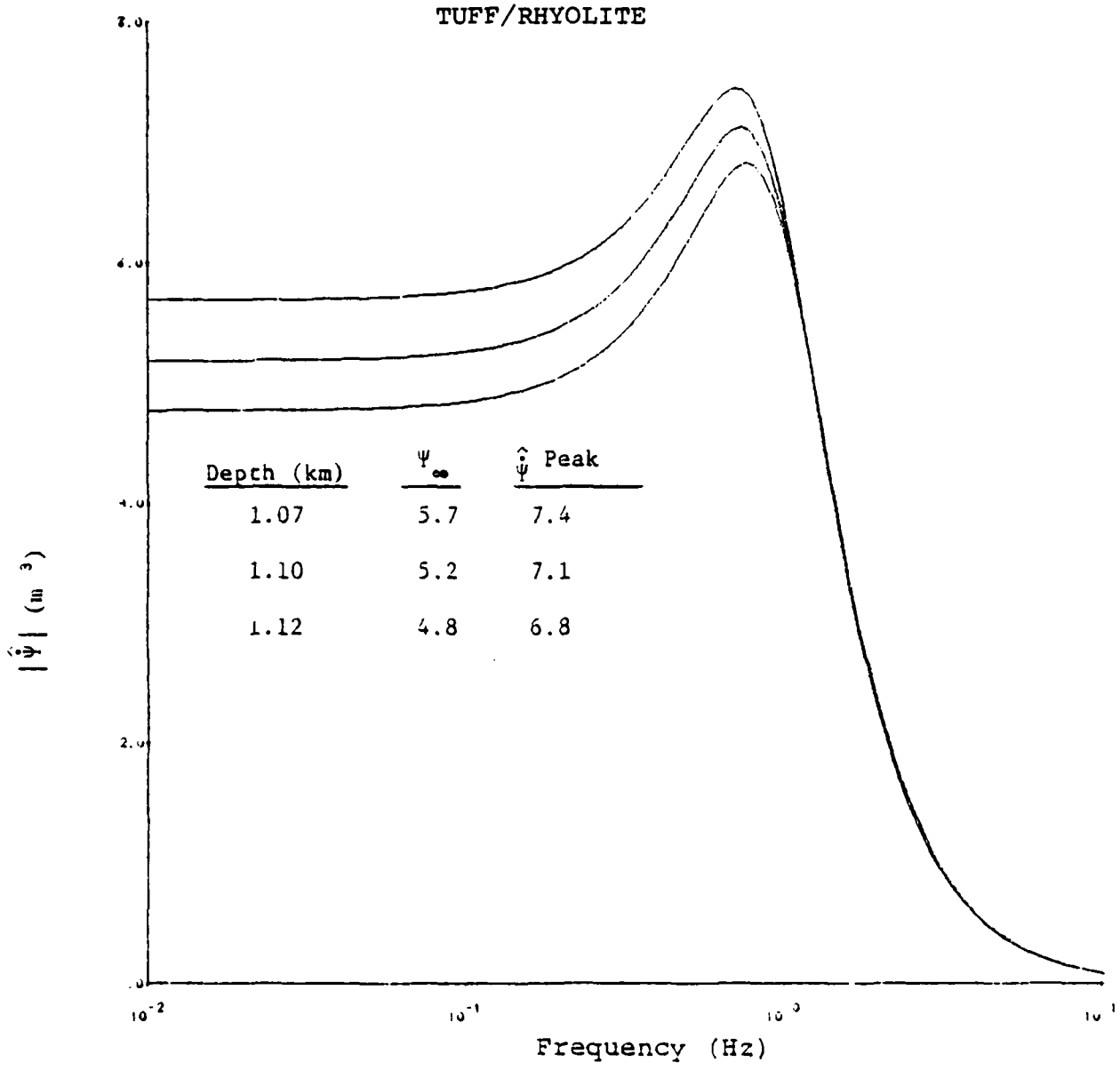

Figure 10. The source functions for three Pahute Mesa explosions are plotted with the amplitude axis scaled to 0.02 KT while the frequency axis is scaled to 600 KT.

TABLE 6. SOURCE REGION CRUSTAL STRUCTURE FOR SYNTHETIC SEISMOGRAM CALCULATIONS

Layer	Depth (km)	Thickness (km)	α (km/sec)	β (km/sec)	ρ (gm/cm^3)
			MAST		
1	0.32	0.32	2.38	1.30	1.66
2	0.67	0.35	3.24	1.90	2.23
3	1.10	0.43	3.90	2.30	2.10
4	1.58	0.48	4.80	2.60	2.65
5	1.72	0.14	4.30	2.40	2.55
6	1.77	0.05	3.85	2.20	2.50
7	2.10	0.32	4.40	2.50	2.58
8	6.00	3.90	4.70	2.60	2.60
9	12.00	6.00	5.40	2.70	2.70
10	20.00	8.00	6.00	3.50	2.80
			CAMEMBERT		
1	0.34	0.34	2.92	1.69	2.00
2	0.42	0.08	4.43	2.56	2.12
3	1.50	1.08	3.50	2.02	2.10
4	2.10	0.60	4.30	2.40	2.60
5-7	Layers 8-10 of MAST structure				
			FONTINA		
1-2	Layers 1-2 of CAMEMBERT structure				
3	0.76	0.34	2.69	1.55	1.93
4	0.91	0.15	2.88	1.66	2.02
5	1.50	0.59	3.31	1.91	2.20
6-9	Layers 4-7 of CAMEMBERT structure				

TABLE 7. RECEIVER REGION CRUSTAL MODEL

Depth (km)	Thickness (km)	α (km/sec)	β (km/sec)	ρ (km/sec)
1.7	1.7	4.0	2.31	2.3
3.0	1.3	5.1	2.94	2.5
20.0	17.0	6.0	3.50	2.8

- Anelastic attenuation was included by the operator (Strick, 1970).

$$\exp\left[-\pi f t^{*}\left(1-\frac{2}{\pi} i \ln\left(\frac{1000}{f}\right)\right)\right]$$

with $t^{*} = 0.8$

- The response of the KS 36000 seismometer was included by a frequency domain operator. The amplitude and phase response are tabulated in Table 8. Woolson (1978) states that there is some ambiguity in the definition of the response of this instrument, in part due to the fact that it is not a minimum phase filter. We point this out as a possible source or error.

We have accumulated much experience with comparing synthetic seismograms computed this way with observed seismograms (e.g., Bache et al., 1975; Bache et al., 1976; Bache, 1977). In most of our previous work the source was a spherically symmetric point source in a layered elastic medium. The important phases are then P and pP which is the P wave times the elastic free surface reflection coefficient. There is, however, a serious question about the accuracy of this representation of pP. Comparison of synthetic and observed seismograms, especially for a wide range of yield, suggest that the actual effect of pP is less than predicted when an elastic pP is assumed.

The explosion source is clearly much more complicated than a spherically symmetric point source. Large amounts of surface spallation are known to occur. Using data from near source gauges, there have been several attempts to estimate the extent of the spalled region (Eisler and Chilton, 1964;

TABLE 8. INSTRUMENT RESPONSE FOR THE KS 36000 SEISMOMETER
(Woolson, Private Communication)

Frequency	Normalized Amplitude	Phase (radians)
0.01	0.59×10^{-5}	-2.175
0.02	0.65×10^{-4}	-2.178
0.05	0.41×10^{-3}	-2.194
0.10	0.265×10^{-2}	-2.279
0.20	0.0165	-2.458
0.40	0.104	-2.777
0.50	0.204	-2.984
0.57	0.287	-3.157
0.67	0.43	-3.393
0.80	0.66	-3.707
1.00	1.00	-4.156
1.11	1.09	-4.325
1.25	1.45	-4.558
1.50	1.80	-4.983
1.67	2.00	-5.238
2.00	2.25	-5.669
2.22	2.35	-5.927
2.50	2.38	-6.225
3.00	2.30	-6.699
3.33	2.11	-6.976
4.00	1.63	-7.396
5.00	1.09	-7.766

Viecelli, 1973; Sobel, 1978). We shall see that the spall impact phase resulting from the estimates made by these authors is large enough to be clearly observable on the teleseismic records.

The synthetic seismogram calculations were done with a composite source including the reduced displacement potential for the explosion and a downward impulse applied at the surface to represent the impulse generated by spall closure. The presence of large amounts of spallation also implies that the pP is not the same as it would be if the material were behaving elastically. We expect some degradation of pP; some loss of energy from this phase. Here we arbitrarily reduce pP by some constant (frequency-independent) factor.

Fixing the path models as we have described, we adjusted the source to achieve a good fit to the observed seismograms. The free parameters that were adjusted are as follows:

1. The P - pP lag time was adjusted within narrow limits imposed by the explosion depth, the known overburden velocities and the observed source-surface travel time. This was done by adjusting the velocities of the overburden layers and/or computing with a source depth that is slightly different than the actual depth.

2. The upgoing waves from the source were multiplied by a constant $\gamma < 1$.

3. A spall impulse given by an amplitude and time lag (with respect to the explosion) was added. These two parameters were adjusted within limits imposed by the empirical estimates of Viecelli (1973) and Sobel (1978). The resulting teleseismic phase is denoted P_s.

Our final synthetic seismograms are shown in Figure 11. The construction of these records is illustrated by separate plots of P (all upgoing source energy was deleted from the calculation) and P + pP. The P_s phase is shown for only the MAST event. Since the source is an impulse, the P_s is the impulse response of the layered earth model and this is nearly the same for all three events.

The comparison between synthetic and observed seismograms is shown in another way in Figure 12. The agreement is remarkably good, especially considering the extremely simple model for spall impact used in the calculation.

The choices for the free parameters used for the synthetics in Figures 11 and 12 are summarized in Tables 9 and 10 where they are compared to independent estimates of these parameters. First, we consider the P-pP lag time data in Table 9. The observed values for mean overburden velocity (measured with small amplitude seismic waves) and source-to-surface travel time (measured at shot time) are not consistent. Both are measures of the velocity of very high frequency waves. The most we would like to say about the P-pP lag time used in the calculations is that it is not inconsistent with the near-source data summarized in Table 9.

The parameters for the spall impulse are summarized in Table 10. We see that the amplitude is between the estimates of Viecilli (1973) and Sobel (1978), which is a reasonable place to be. The delay time we found necessary to match the data is a bit shorter than the estimates given by these authors, but not by too much.

An m_b is given for each seismogram in Figures 11 and 12 except the P_s record. This m_b was determined with the semi-automated time domain procedure described in Section II. The phase measured is first trough to second peak in each case. Concerning this m_b, we see the following:

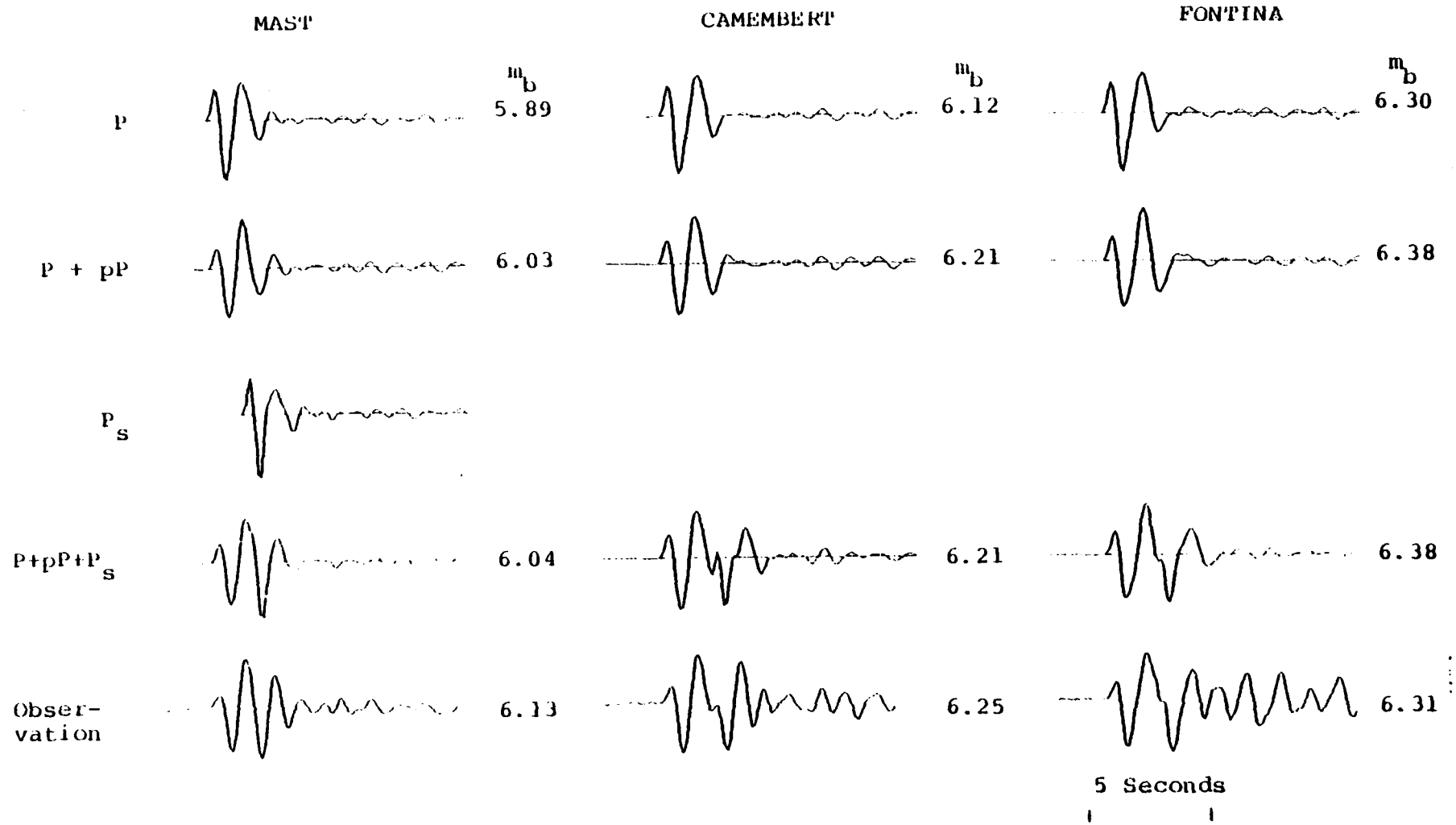

Figure 11. Construction of theoretical seismograms at HNME for three Pahute Mesa explosions.

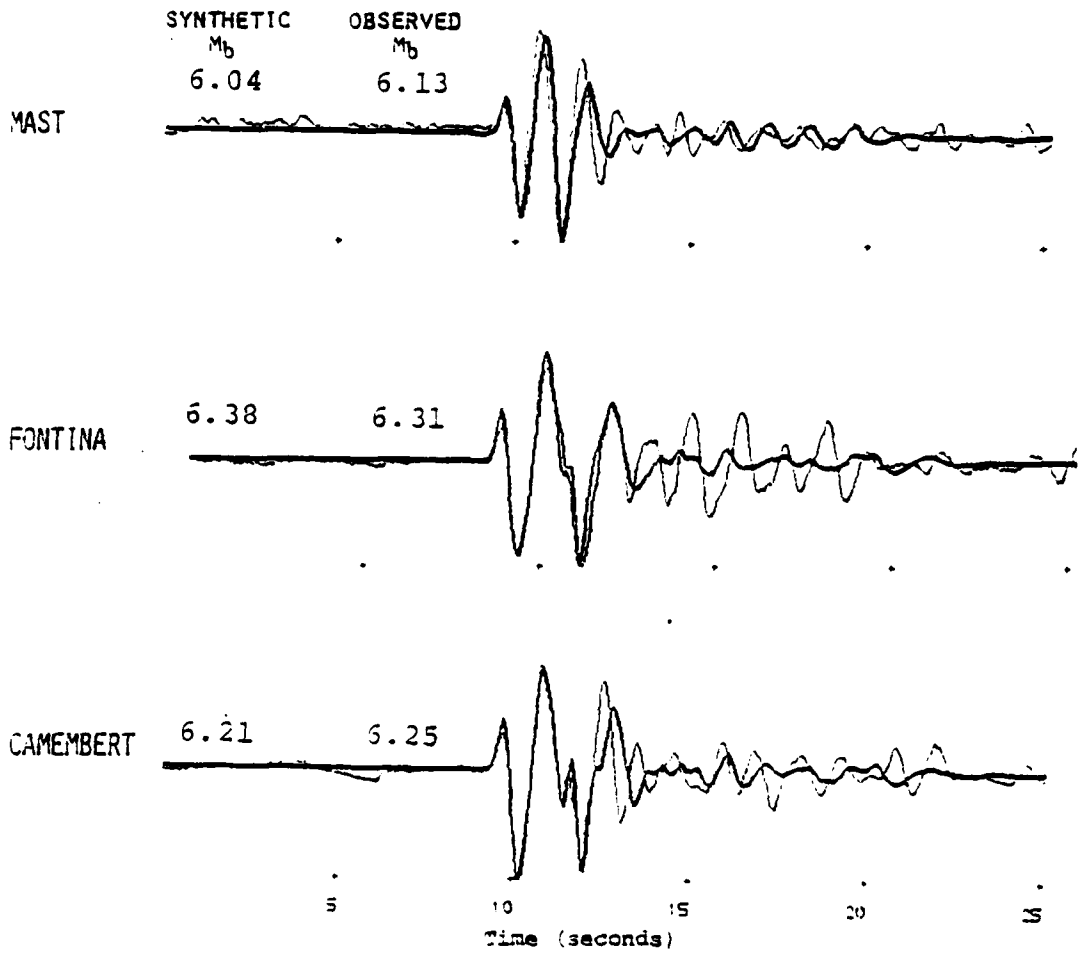

Figure 12. Comparison of synthetic (heavy lines) and observed seismograms.

TABLE 9. PARAMETERS FOR THE P-pP LAG TIME IN THE SYNTHETIC SEISMOGRAM CALCULATIONS

	MAST	CAMEMBERT	FONTINA
Theoretical parameters			
Depth of burial (km)	1.07	1.10	1.18
P-pP lag (sec)	0.67	0.63	0.76
Mean overburden velocity (km/sec)	3.10	3.35	2.99
Mean overburden density (gm/cm^3)	2.01	2.07	2.04
Source-surface travel time (sec)	0.34	0.33	0.39
Observed Data (Tables 1-3)			
Actual depth (km)	0.91	1.31	1.22
Mean overburden velocity (km/sec)	3.88	2.90	2.86
Mean overburden density (gm/cm^3)	2.24	2.10	2.00
Source-surface travel time (sec)	0.36	0.45	-
Depth/mean overburden velocity (sec)	0.23	0.45	0.43

TABLE 10. PARAMETERS FOR THE P_s PHASE IN THE SYNTHETIC SEISMOGRAM CALCULATIONS

	MAST	CAMEMBERT	FONTINA
Spall Impulse (Dyne-sec/km)	10×10^{14}W	14×10^{14}W	9×10^{14}W
$P-P_s$ lag time (sec)	1.25	1.92	1.86
γ*	0.60	0.50	0.50

Estimated of spall impulse from near-field data

Viecelli (1973): 4.6×10^{14}W

Sobel (1978): $21\text{-}25 \times 10^{14}$W

Estimated of $P-P_s$ delay from near-field data:

2.0-2.5 seconds

*Factor multiplying the upgoing waves from the source.

- The pP phase enhances the m_b compared to that for P alone. This enhancement is less than would occur with these P-pP lag times if we had not reduced the size of the pP phase by about half.

- The P_s phase has almost no effect on the time domain m_b.

- While this is not the purpose here, we note that the agreement of observed and synthetic m_b is quite good. This gives confidence in our source and path models.

In this report we do not want to make too much of the interpretation of the prominent later phase as being generated by spall closure. There are alternative explanations for this secondary phase. From the data at one station we cannot be sure it is not a multipathing phenomenon. Also, there are other source effects that could generate such a phase. Tectonic strain release is one that comes to mind. However, our previous work (Bache, 1976) indicates that the tectonic release component can only be this large for the most favorable source orientation-station azimuth combinations. Again, we must look at data from other stations to see if tectonic strain release is a plausible explanation.

Our objective here is to generate synthetic seismograms that closely resemble the data so we can better understand our $\hat{m}_b$ algorithm. Using the spall impulse model to generate a phase with the right time delay and amplitude, we have accomplished that objective. More detailed discussion of the physical nature of this phase will be given in a separate report.

We now show the results of applying our $\hat{m}_b$ algorithm (Section III) to the synthetic seismograms of Figure 11. The plots of log $(A_k \cdot f_k)$ and t_g versus f_k are shown in Figure 13 for the synthetic seismograms and for the observations. The algorithm used to obtain these plots is described in Section 3.3.

The calculation of $\hat{m}_b$ from the log $(A_k \cdot f_k)$ and t_g data is described in Section 3.3. We begin by obtaining the peak value of log $(A_k \cdot f_k)$. This is indicated by an asterisk on the plot. We then define the upper and lower limits of an f_k band about the f_k at the peak. These limits are chosen such that the t_g is within one second of the t_g at the peak log $(A_k \cdot f_k)$. The limits chosen automatically by this algorithm are indicated on the synthetic P + pP + P_s and observed seismograms in Figure 13 by small vertical bars. For the P and pP synthetics for each event the f_k limits were forced to be the same as for the P + pP + P_s. This was done so we could see the effect of adding the individual phases without being mislead by averaging over different bands.

From the data plotted in Figure 13 we compute $\hat{m}_b$ from

$$\hat{m}_b = \log A + 3.48 \quad , \tag{A.1}$$

where

$$A = \frac{1}{\Delta f_k} \int_{\min f_k}^{\max f_k} (A_k \cdot f_k)\, df_k \quad , \tag{A.2}$$

and $\Delta f_k = \max f_k - \min f_k$, the f_k band indicated on the plots. On each of the nine plots in Figure 13, we give the $\hat{m}_b$ values computed from the above equations.

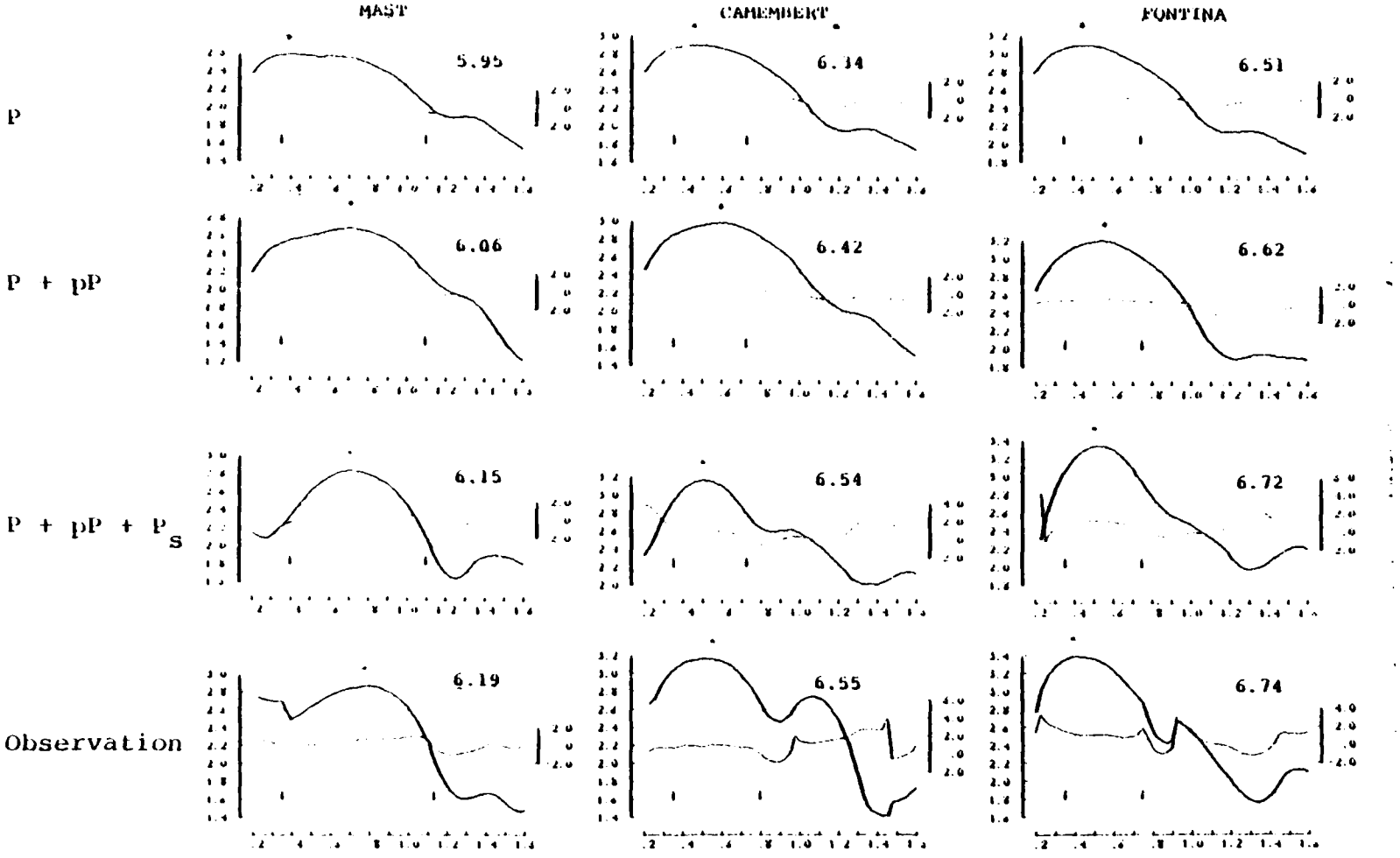

Figure 13. Log ($A_k \cdot f_k$) and t_g versus f_k for the synthetic seismograms of Figure 11.

In Figure 14 we again show the full (P + pP + P_s) synthetics with the t_g time band for the $\hat{m}_b$ calculation indicated on each seismogram. The asterisk denotes the t_g associated with the peak log ($A_k \cdot f_k$), which is also denoted by an asterisk in Figure 13. The bars indicate the maximum and minimum t_g within the band. We see that the identified arrival time for the energy contributing to $\hat{m}_b$ is near the front of the record where conventional time domain m_b measurements are made. However, since the width of the filter is about four seconds (defined as ± one standard deviation, see Figure 10 in Section 3.3), energy arriving outside the band indicated in Figure 14 contributes to the $\hat{m}_b$.

The m_b values from Figure 11 and the $\hat{m}_b$ from Figure 13 are summarized in Table 11. From the data in this table and the figures, we draw the following conclusions about $\hat{m}_b$:

- The agreement of observed and synthetic m_b is remarkable, and that for $\hat{m}_b$ is even better.

- Comparing P and P + pP, the m_b and $\hat{m}_b$ differences are the same. Thus the pP phase seems to have about the same effect on both magnitude measures, at least for this depth range.

- The P_s phase has no effect on m_b. However, it enhances the $\hat{m}_b$ by about 0.10 units.

- Considering the width of the time domain filters and the t_g associated with the amplitudes used to compute $\hat{m}_b$ (Figure 14), the effect of the P_s phase on $\hat{m}_b$ is to be expected.

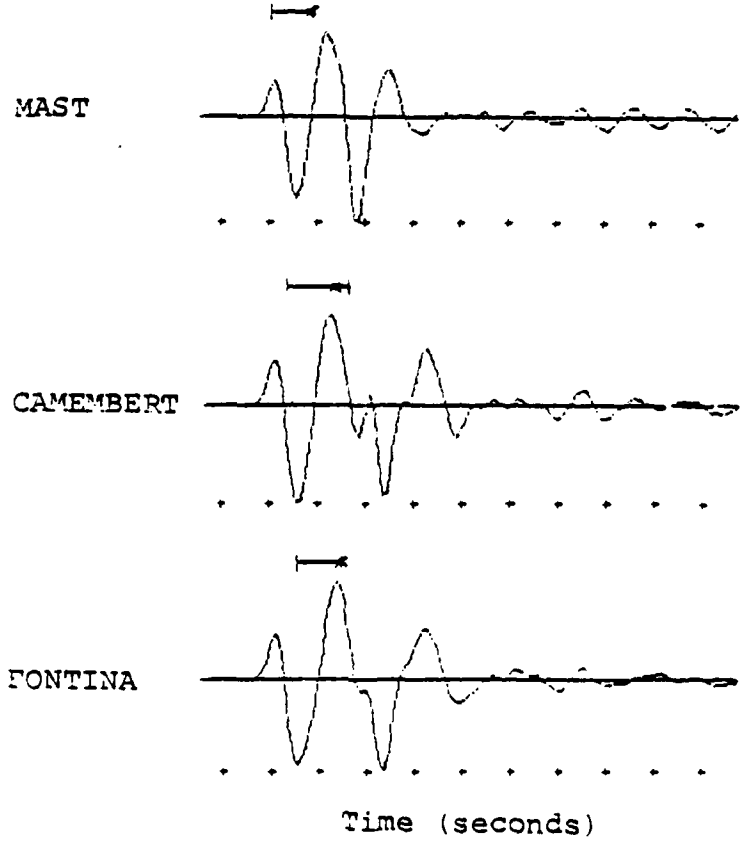

Figure 14. The P + pP + P_s synthetic seismograms from Figure 11 are shown with marks indicating the t_g time band for the $\hat{m}_b$ determination.

TABLE 11. SUMMARY OF m_b AND $\hat{m}_b$ DATA

Seismogram	m_b (Figure A.2)	$\hat{m}_b$ (Figure A.4)
MAST		
P	5.89	5.95
P + pP	6.03	6.06
P + pP + P_s	6.04	6.15
Observed	6.13	6.19
CAMEMBERT		
P	6.12	6.34
P + pP	6.21	6.42
P + pP + P_s	6.21	6.54
Observed	6.25	6.55
FONTINA		
P	6.30	6.51
P + pP	6.38	6.62
P + pP + P_s	6.38	6.72
Observed	6.31	6.74

- From the plots in Figure 13 we can infer the significance of the spectral holes in the log $(A_k \cdot f_k)$ plots for the observed seismograms. They are almost certainly due to the presence of P_s. The resolution of the narrow band filters is not nearly fine enough to see effects of the P - pP interference.

V. THREE-DIMENSIONAL FINITE DIFFERENCE EARTHQUAKE MODELING

5.1 INTRODUCTION

In this section, we summarize and discuss the results of our earthquake modeling with the ILLIAC, using TRES, a three-dimensional finite difference code (Cherry, 1977). We modeled faulting as a propagating stress relaxation due to shear failure on a planar surface. Ultimately, we would like to specify the relevant physical properties of the medium and its initial conditions, and allow a mathematical model of failure to determine the subsequent evolution of the fault plane. However, at this stage, we have not addressed the physical mechanism of failure. Instead, we prescribe the propagation of the fault surface, and boundary conditions on the fault surface are governed by a simple Coulomb friction law.

While the TRES algorithm is quite flexible in the allowed specification of geometry and material behavior, the version currently operational on the ILLIAC is somewhat restricted. The faulting must nucleate from a point and propagate with circular symmetry until reaching the edges of a rectangular fault plane. There are no material boundaries other than the fault plane; that is, the calculations are done in a whole space. The material behavior is linearly elastic except in the vicinity of the fault plane where plastic yielding is permitted.

We performed two three-dimensional finite difference calculations for this study. Details of the fault model are given by Day, et al. (1978). The two calculations differed only in the yield strength Y assigned the material. Both calculations were for a square fault plane in a uniform whole space, with rupture initiated at the center of the square fault (Figure 15). The following parameters were employed for both calculations:

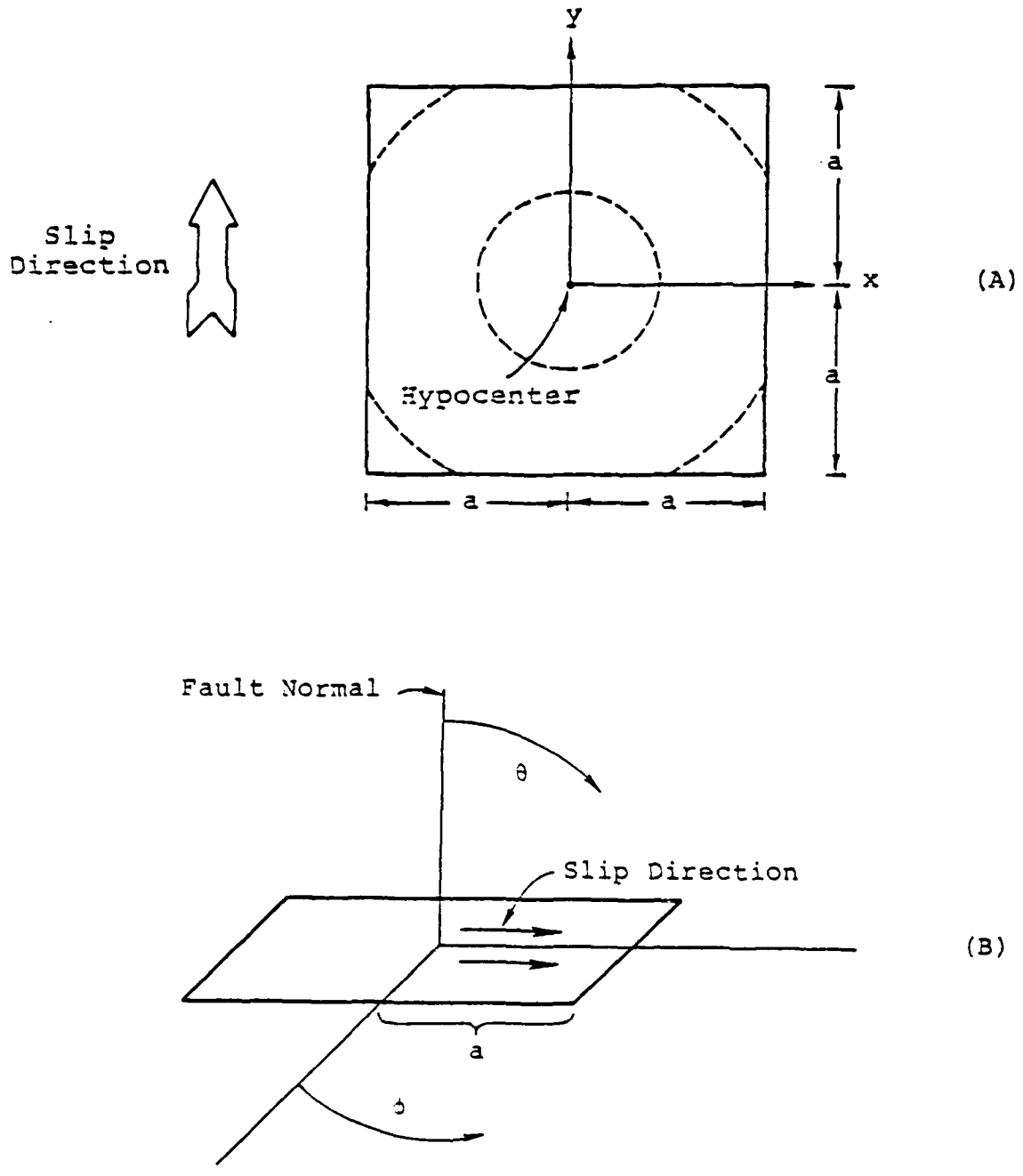

Figure 15. (A) The fault configuration for the finite difference simulation, and (B) the coordinate system for describing the radiated field.

P wave velocity	α = 5.93 km/sec
S wave velocity	β = 3.42 km/sec
Density	ρ = 2.74 gm/cm
Rupture velocity	V_R = 3.08 km/sec
Tectonic shear stress	σ_T = 1 kbar
Frictional stress	σ_f = .82 k bars
Fault dimensions	2ax2a = 3 km x 3 km

For the first finite difference calculation, the "elastic" model, the yield strength Y was set to infinity, so the constitutive model was linearly elastic. For the second finite difference calculation, the "plastic" model, Y was set to $\sqrt{3}\sigma_T$, so that the fault zone was initially stressed to the failure surface. With this choice of Y, plastic flow ensues when the second deviatoric stress invariant J_2 increases above its initial value. This dissipates any dynamic shear stress concentration ahead of the crack tip. Plastic yield was permitted only within 0.2 km of the fault plane; elsewhere linear elasticity was employed.

For both the elastic and plastic fault problems, the medium was represented by cubic finite difference zones 0.1 km on a side. The numerical grid was large enough that no reflection from the exterior grid boundary returned to the fault zone during the calculation.

These initial calculations permit us to examine the accuracy of the three-dimensional numerical method, investigate the near- and far-field signal froma a simple propagating stress-relaxation model, and clarify the physical interpretation of the parameters of the Archambeau spherical source model. The inclusion of plastic yielding in the second calculation is a significant step toward incorporating realistic rock mechanics into the fault model, and we examine its effect on the near- and far-field signals.

5.2 SUMMARY OF RESULTS

The main results of these two calculations are summarized here; for details, we refer to Day, et al., (1978).

5.2.1 Comparison of an Analytic Solution

Kostrov (1964) obtained an analytical solution for the problem of a circular crack which nucleates at a point in a homogeneous, unbounded elastic medium and expands at a constant rupture velocity without stopping. This problem corresponds exactly to the conditions of the elastic model considered in this study, until time a/V_R, where a is the half-length of the square fault. We can compare the initial fault slip, obtained numerically, to Kostrov's analytic solution, although once the rupture front reaches the edge of the square fault plane and stops growing, we expect the numerical solution to begin to deviate significantly from Kostrov's solution.

Figure 16 shows the slip obtained at several points in the fault plane. The dashed curves are the finite difference solution and the solid curves are the analytic solution. The vertical bars indicate the arrival times of edge effects due to stopping of the rupture at its outer boundary. The two solutions display the anticipated agreement at each point prior to the arrival of the edge effects. The small deviation of the numerical solution from the analytic solution at early time results, at least partially, from imprecise weighting of the stress drop to account for the fractional rupture of a finite difference zone by the circular rupture front. Archuleta and Frazier (1978) achieved somewhat better agreement with Kostrov's solution by incorporating fractional rupture into their finite element scheme.

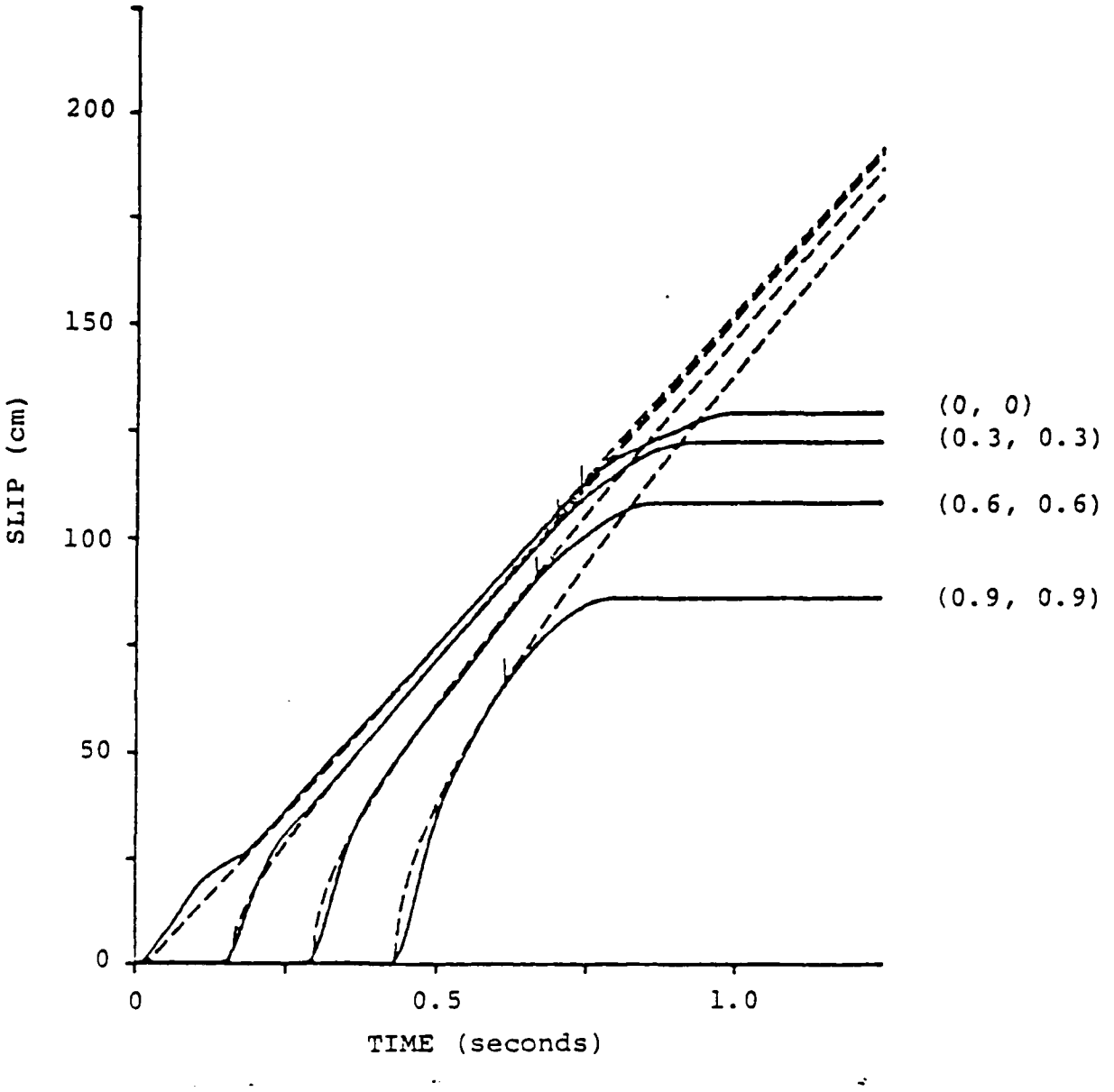

Figure 16. Relative displacement on the fault for the elastic case. The dashed curves are Kostrov's analytic solution; the solid curves are the finite difference results. x,y coordinates in kilometers are given in parenthesis. Vertical lines indicate the arrival times of edge effects due to fault finiteness.

5.2.2 Stress History Near the Fault

Figure 17 depicts the stress histories near the fault plane for the two models (the purely elastic model and the plastic model). The shear stress in the direction of prestress (σ_{yz}) is plotted versus time for seven points along the fault plane diagonal, at increasing distance from the hypocenter. The stresses shown are actually evaluated at the finite difference zone centers adjacent to the fault, which are 0.05 km from the fault plane.

First, consider the stress for the elastic problem shown in Figure 17. Initially, the stress at a given point is at the prestress level (1 kbar). Prior to the rupture front arrival at a given location, the stress increases above the prestress level. This stress concentration ahead of the rupture front is a general characteristic of elastodynamic cracks with subsonic rupture propagation. We note the amplification of this stress concentration with increasing distance in the direction of rupture. At the rupture arrival time, the stress drops abruptly, over-shooting and then settling at the prescribed frictional stress of 820 bars. The over-shoot results from the fact that the observation points are slightly removed from the fault plane itself. The same phenomenon is present in Richards (1976) analysis of the self-similar expanding crack. The stress then remains at the frictional stress level until the nearby part of the fault plane heals. Then the stress relaxes to a value less than that of kinetic friction. The fault over-shoots the static equilibrium value of slip. The healing wave shows up clearly in Figure 17; it propagates toward the hypocenter from the periphery of the fault. The last phase evident in the figure propagates outward from the hypocenter, and this phase corresponds to the shear wave associated with the final arrest of slip at the center of the fault.

Now consider the stresses for the plastic problem in Figure 17. Until healing occurs at a given point, the stress history is unchanged from the elastic case except that the

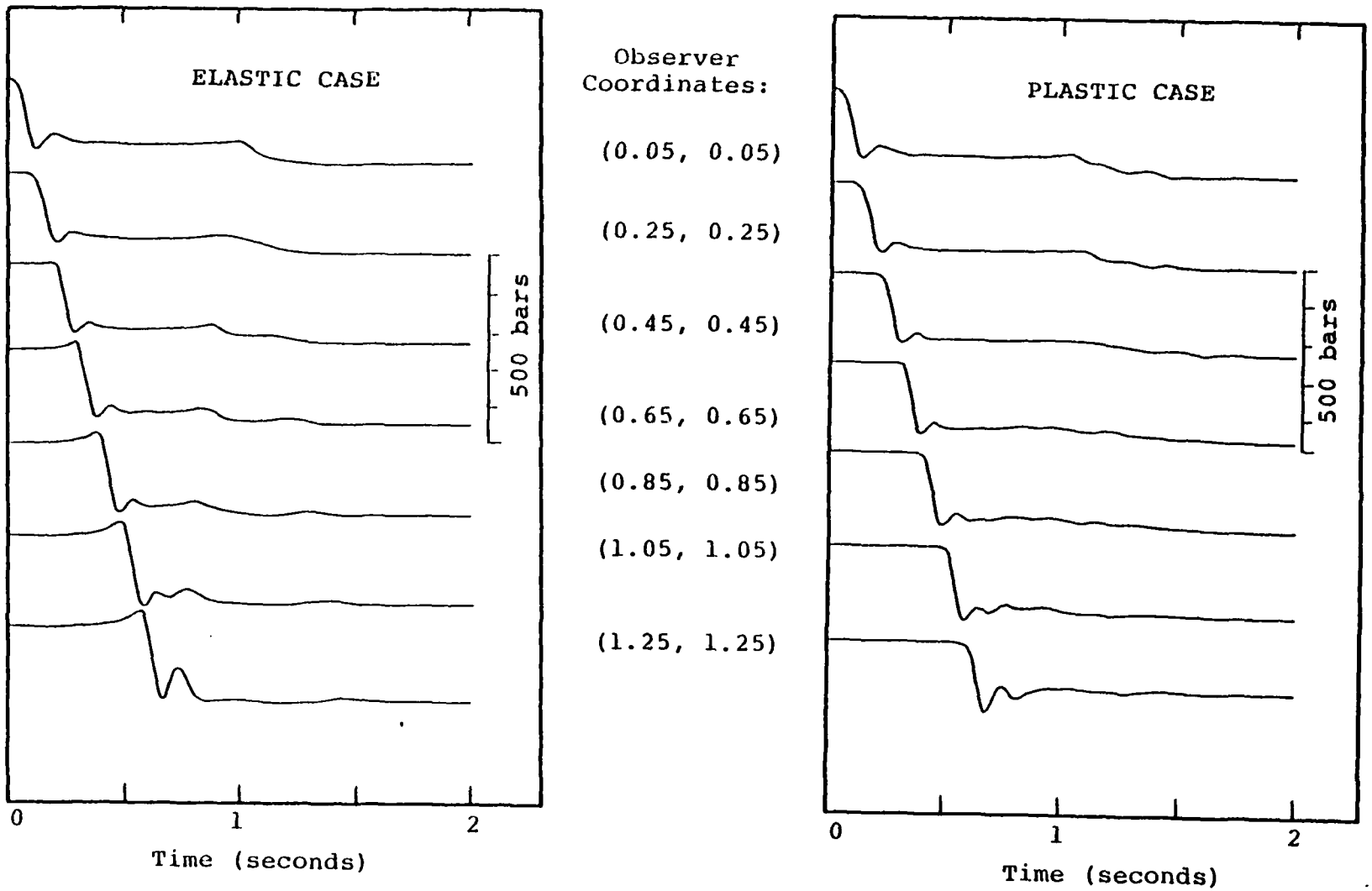

Figure 17. Time histories for the stress component σ_{yz} adjacent to the fault plane, for several hypocentral distances. Observation points are at a distance of 0.05 km from the fault plane; x and y coordinates are shown in parenthesis.

stress concentration ahead of the rupture front has been eliminated. After healing, the residual stress is nearly the same as in the elastic case.

Figure 18 displays the stress σ_{yz} near the fault plane as a function of azimuth ϕ. Again, the stress is zone centered, so it is actually evaluated at points 0.05 km displaced from the fault plane. The five points displayed are at approximately the same distance, 1.15 km, from the center of the fault. The stress concentration proceding rupture is nearly zero (actually slightly negative) at $\phi = 0°$, and increases smoothly to a maximum at $\phi = 90°$. This pattern can be compared to Figure 8 of Richards (1976). The stress histories are very similar, although his results are for an elliptical fault in which rupture velocity varies with azimuth from 0.92 β to β, whereas our numerical solution is for circular rupture propagation at rupture velocity 0.9 β.

Figure 19 shows the stress component σ_{yy} along the fault plane. This component of stress is not relieved by plastic flow, and the concentration of σ_{yy} ahead of the rupture is essentially identical in both the plastic and the elastic cases.

5.2.3 Velocity History on the Fault

Figure 20 shows the slip velocity obtained on the fault plane at increasing distances from the hypocenter along a radial line. The solid curves are for the elastic case, the dashed curves are for the plastic case.

It is evident from Figure 20 that the initial velocity is strongly peaked and the peak value increases with hypocentral distance. We can understand this characteristic of the velocity curves by means of Kostrov's analytic solution,

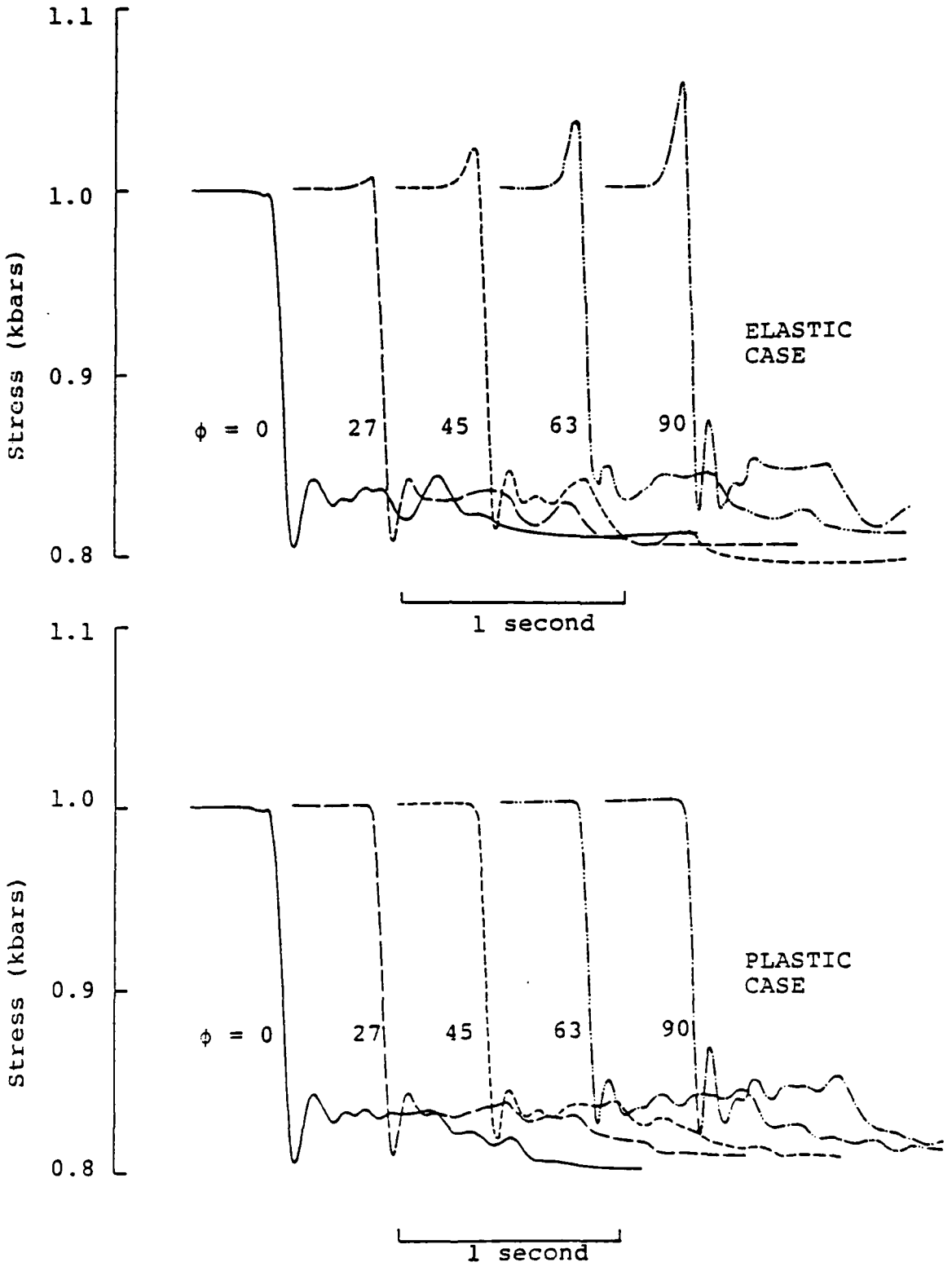

Figure 18. Time history of σ_{yz} adjacent to the fault plane for several azimuthal angles ϕ. Each observation point is at a distance 0.05 km from the fault plane, and a distance 1.15 km from the center of the fault.

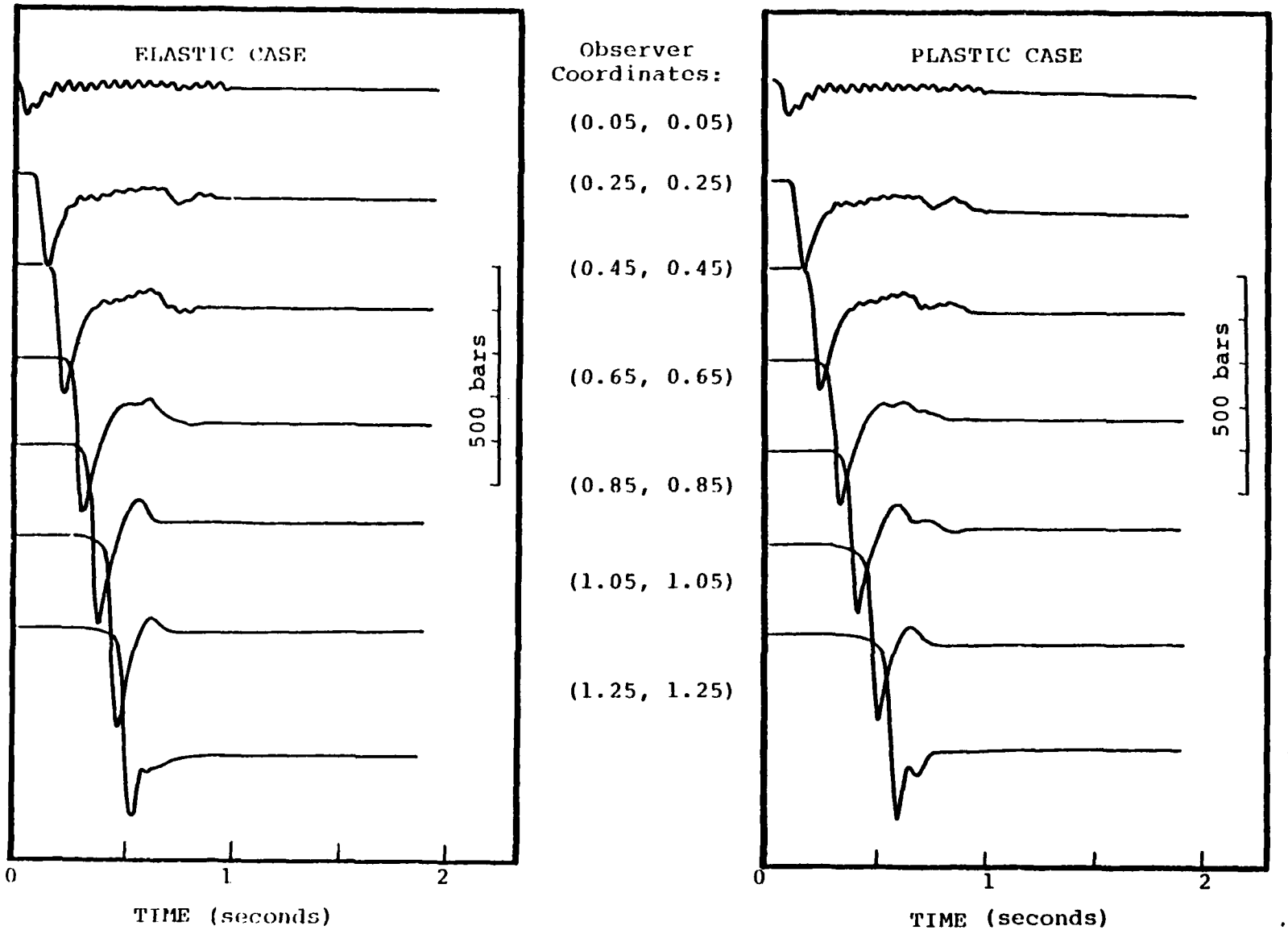

Figure 19. Time history of σ_{yy} along the fault plane. Observation points are as in Figure 17.

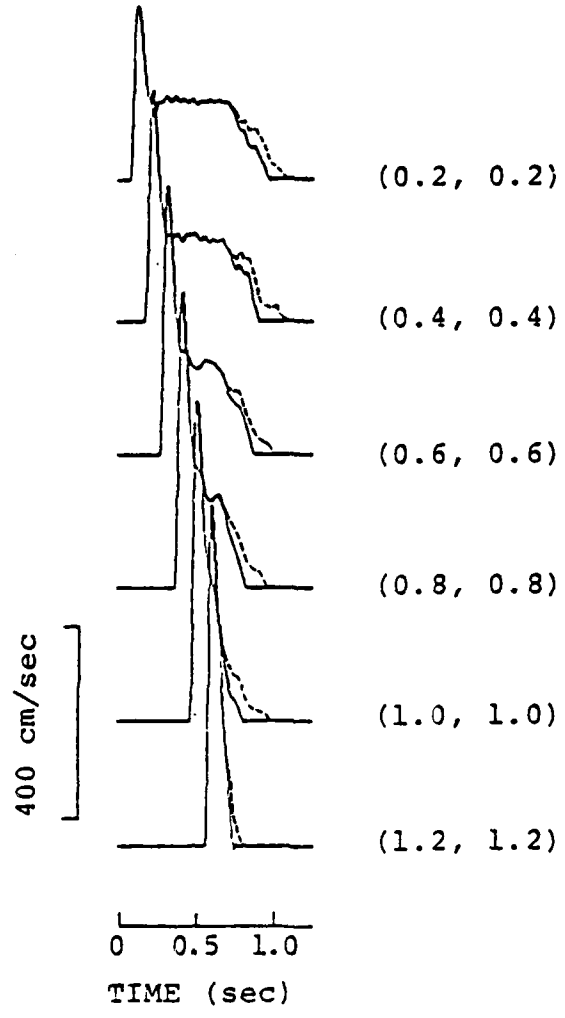

Figure 20. Slip velocity in the fault plane. Solid lines are the elastic case, dashed lines the elasto-plastic case. x,y coordinates in kilometers are shown in parenthesis.

which predicts that peak slip velocity should increase as the square root of the hypocentral distance. This prediction is in good agreement with the numerical results in Figure 20.

It is evident from Figure 20 that the initial part of the particle velocity is unaffected by the introduction of plasticity, within the resolution of the finite difference calculation. A large velocity peak occurs at the crack tip, even in the absence of the strong stress concentration associated with the purely elastic problem. The plastic and elastic solutions are indistinguishable until the arrival of the stopping phase.

After the arrival at a given point of edge effects due to stopping of the rupture front, the fault plane velocities are substantially modified by the plasticity. As Figure 20 indicates, yielding at the crack tip smooths the stopping phase, robbing the slip function of high frequencies and increasing the long-period content of the slip function. The average static slip on the fault plant is increased by about 11 percent when yield is permitted.

5.2.4 Radiated Fields

The average slip for the elastic fault was 79 cm, which is 0.61 times the value of slip at the center of the fault. The seismic moment obtained from this average slip was 2.28×10^{24} dyne-cm. This value is 14 percent greater than the prediction obtained by combining the static circular crack formula (Keilis-Borok, 1959) with the expression for seismic moment, $M_o = \mu A \bar{s}$. This over-shoot of the static solution has been observed in previous dynamic modeling — notably the work of Madariaga (1976).

Figures 21 and 22 present normalized far-field P and S wave displacement spectra and time histories for the elastic

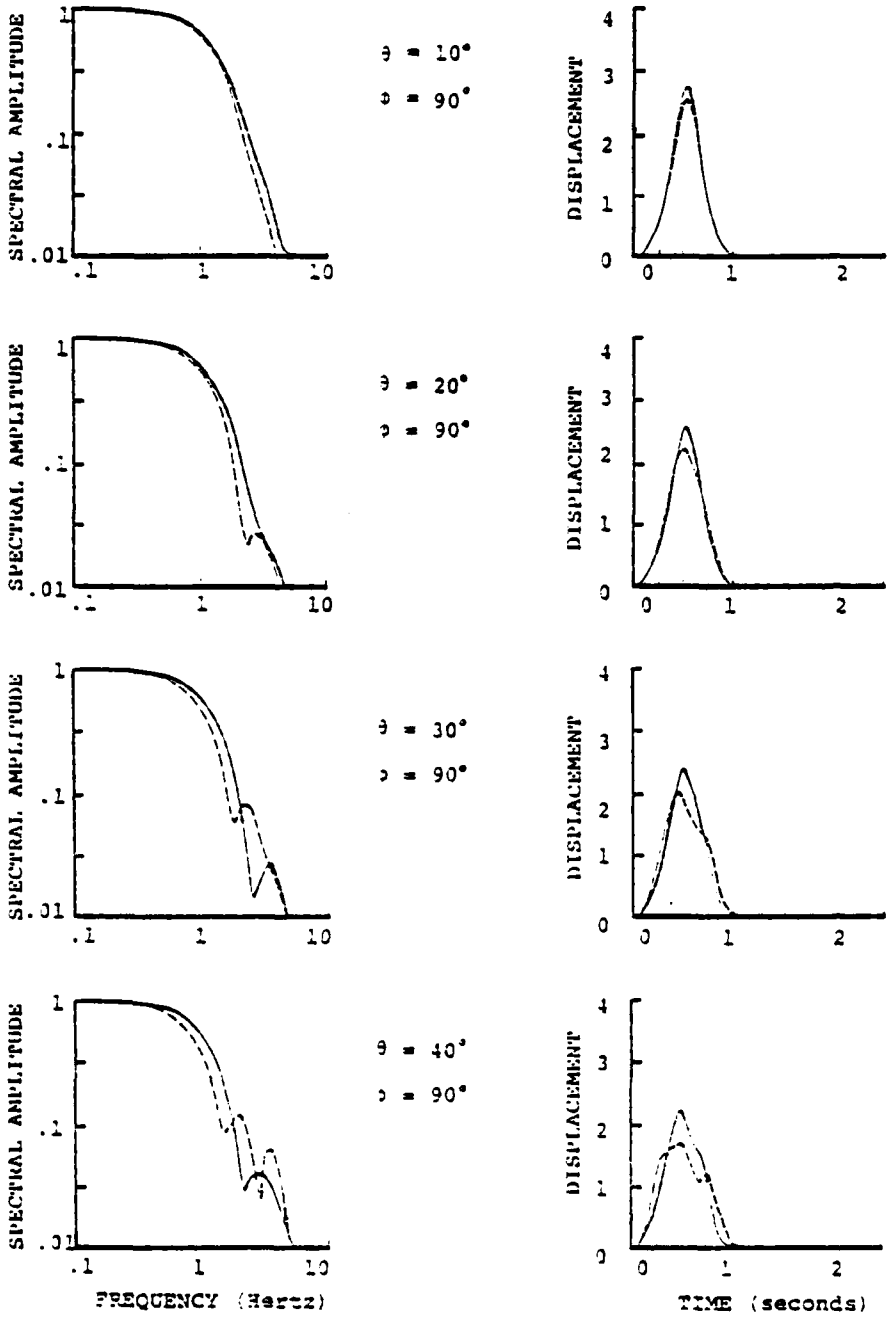

Figure 21. Normalized far-field P wave (solid curves) and S wave (dashed curves) displacement spectra and time histories. Displacements are shown at 10° intervals in θ, for ϕ = 90°.

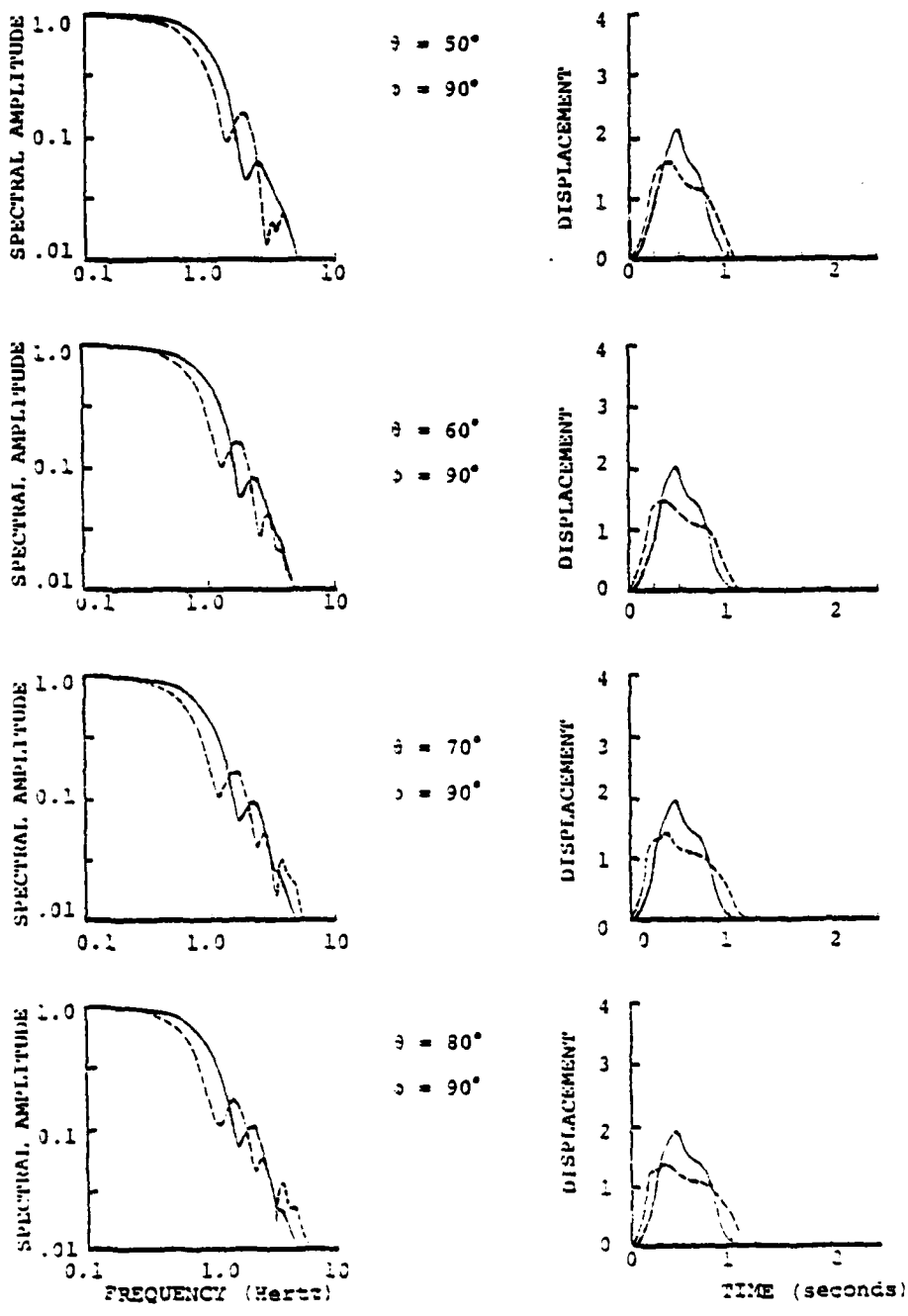

Figure 21. (Continued)

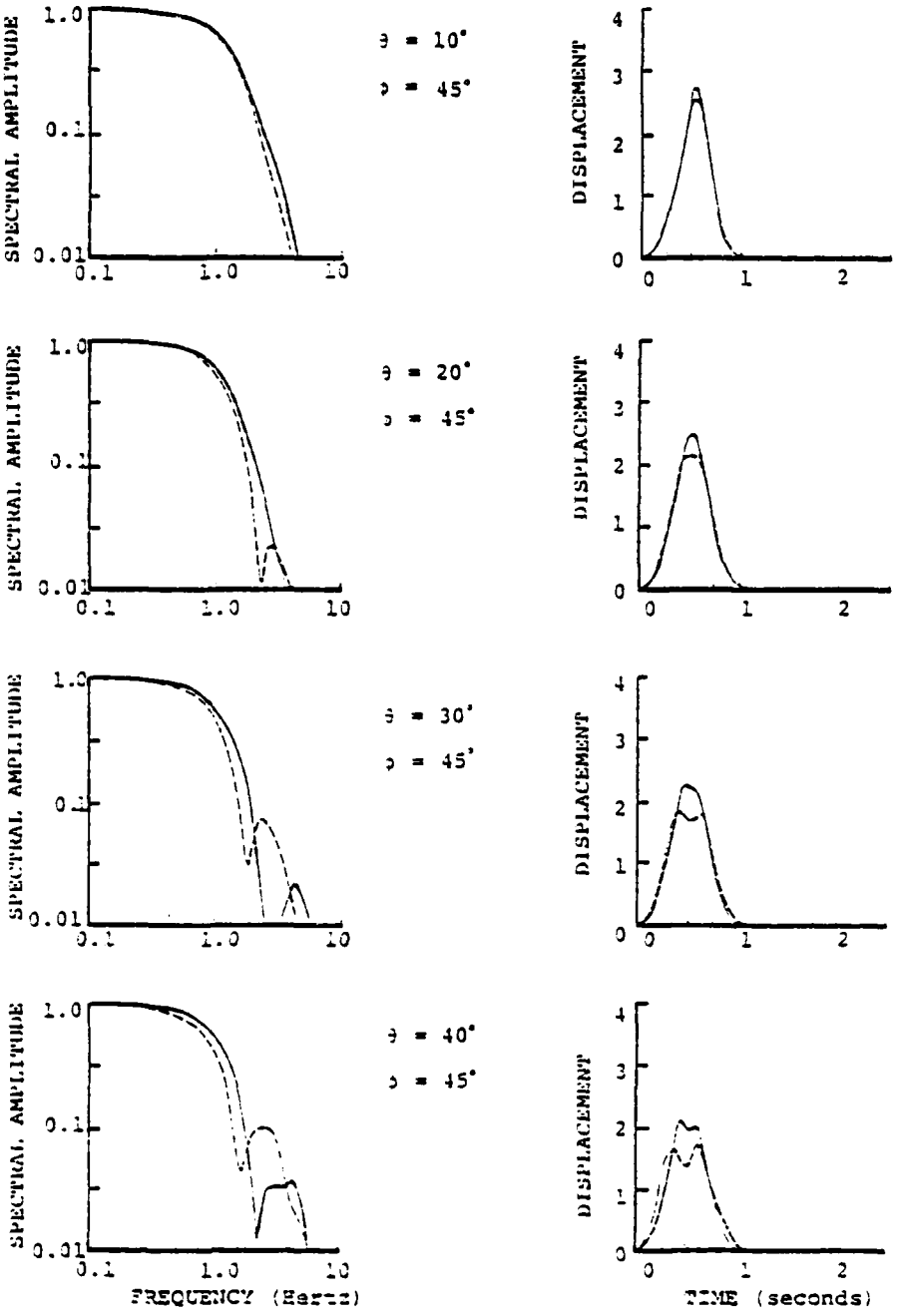

Figure 22. Normalized far-field P wave (solid curves) and S wave (dashed curves) displacement spectra and time histories. Displacements are shown at 10° intervals in θ, for ϕ = 45°.

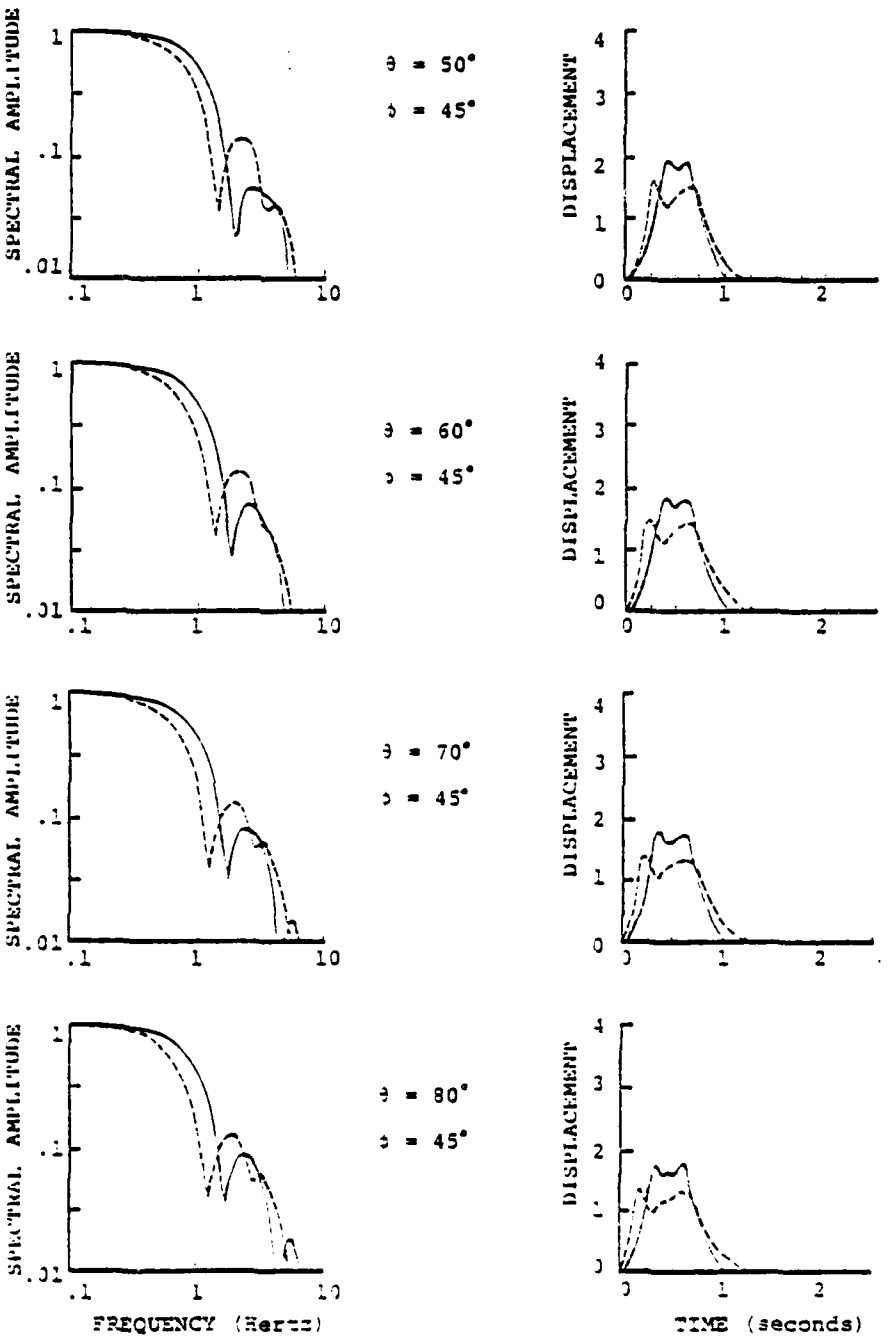

Figure 22. (Continued)

case. Results are shown at 10° intervals in θ; Figure 21 is for $\phi = 90°$, and Figure 22 is for $\phi = 45°$. Solid lines are the P wave displacements, dashed lines are the S wave displacements. The curves are normalized by the zero frequency spectral amplitude, derived from the average slip $\tilde{s}$. For P waves, the normalization is $\beta^2/\alpha^2 \tilde{As} (4\pi \alpha r)^{-1} R_p$. For S waves, we can interpret the curves either as the θ component of displacement normalized by $\tilde{As} (4\pi \beta r)^{-1} R_{s\theta}$, or as the ϕ component of displacement normalized by $\tilde{As} (4\pi \beta r)^{-1} R_{s\phi}$. R_p, $R_{s\theta}$ and $R_{s\phi}$ are double couple radiation patterns (see Day, et al. 1978), A is the fault area, and r the hypocentral distance. The travel times from hypocenter to receiver have been removed from the P and S time histories.

Comparing results at $\phi = 90°$ with those at $\phi = 45°$, we note that pulse width and corner frequency have practically no dependence on ϕ; at higher frequency there is some difference in spectral and time domain detail between the 2 azimuths. (Results at $\phi = 0°$ are virtually identical to those at $\phi = 90°$, and are not shown.)

Dependence of pulse width and corner frequency on θ and on wave type (P or S) is significant. Our observations concur with those of Madariaga (1976):

(a) S wave corner frequencies are smaller than P wave corner frequencies, except near $\theta = 0°$.

(b) Pulse width and corner frequency are governed by the travel time difference between stopping phases from the near and far edges of the fault. Thus, pulse width increases with θ, being greatest for observers near the plane of the fault and smallest for observers near the fault normal.

(c) P and S wave corner frequencies, for $\theta > 30°$, are expressed very well by Madariaga's Equation (24), replacing the circular fault radius with the square fault half-width.

The average static slip for the plastic fault problem is 88 cm, which exceeds the average slip in the elastic case by 11 percent. This results from the smoothing of the stopping caused by yielding at the fault edge. Actually, this is precisely the percentage increase that would be predicted by simple scaling of the elastic problem for a fault dimension occupying the entire length and width of the plastic zone (the plastic zone extended 0.2 km beyond edge of the fault).

The seismic moment for the plastic problem is 3.15×10^{24} dyne-cm, which is 38 percent larger than the moment for the elastic case. Scaling of the elastic solution as suggested in the last paragraph would predict a slightly larger increase in moment, 42 percent instead of 38 percent.

Figure 23 shows the effect of plastic yield on the far-field displacements. Spectra and pulses are shown at $\phi = 90°$ for 3 values of θ: S wave solutions are shown at $\theta = 0°$ and $\theta = 90°$, and P wave solutions are shown at $\theta = 45°$. Dashed curves are the elastic case, solid curves the plastic case. In each case, the far-field solution is the sum of multipolar terms up to $\ell = 8$.

The main influence of plastic yielding is to smooth the stopping phases, with the result that the low-frequency part of the spectrum is enhanced at the expense of the high frequency part of the spectrum. Consider for example, the P wave pulse at $\theta = 45°$. Two stopping phases, corresponding to rupture arrival at the near and far edges of the fault,

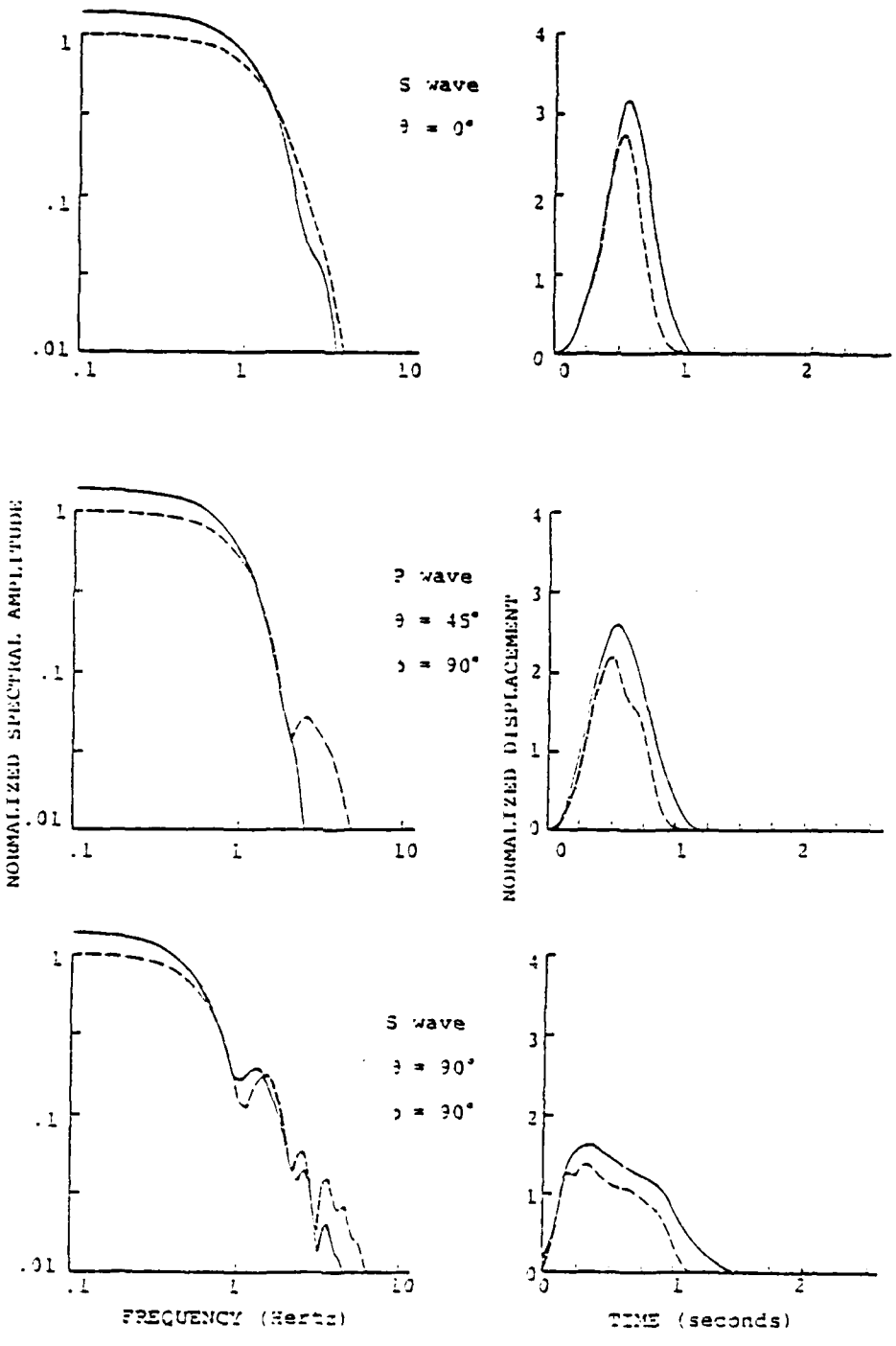

Figure 23. Comparison of displacement spectra and time histories from the plastic problem (solid curves) with those from the elastic problem (dashed curves).

respectively, are apparent in the P wave displacement pulse for the elastic problem. These appear as discontinuities in slop occurring at about 0.46 seconds and 0.67 seconds. The P wave pulse for the plastic problem coincides with that for the elastic problem until the arrival of the first stopping phase. The displacement pulse for the plastic case then reverses more gradually, over-shooting the elastic case; the second stopping phase is almost imperceptible for the plastic case.

Clearly, the increase in seismic moment is the consequence of plastic strain induced at the periphery of the slip surface. Relieving stress by permitting plastic strain is very similar to relieving stress by permitting frictional sliding, but with the frictional stress approximately equal to $Y/\sqrt{3}$ (which in this case equals the prestress σ_T). Outside the zone in which yielding was permitted, a static shear stress concentration about 23 percent in excess of the prestress developed. Thus, if a larger plastic zone had been specified, the seismic moment would have been even greater, as plastic strains extended outward to eradicate the stress concentration. On the other hand, had a somewhat higher yield strength been specified, the results of the plastic problem would have approached those of the elastic case. If the yield papameter $Y/\sqrt{3}$ had exceeded the tectonic stress by 1.44 $(\sigma_T - \sigma_f)$ (that is, if Y had been 26 percent larger), no yielding would have occurred, and the two solutions would have been indistinguishable.

5.2.5 Comparison to Radiation from an Archambeau-Minster Source

As a generator of teleseismic signals, the Archambeau-Minster source model possesses several of the relevant features expected of earthquake sources. We compared synthetic short-period teleseismic P waves generated by a bilateral version

of the Archambeau-Minster source model with those generated by the elastic fault model. The bilateral Archambeau source consists of two independent, adjacent spherical sources, propagating in opposite directions. For the comparison, both models were scaled to have the same seismic moment, and the cross-sectional area of the Archambeau-Minster spherical volumes was made equal to the area of the square fault plane (9 km). Thus, the maximum source dimension was somewhat larger for the spherical source.

In Figure 24 we compare five short period teleseisms from the elastic finite difference calculation to those from a bilateral version of the Archambeau model. The amplitude (corrected for period-dependent instrument response) and period data from these synthetic seismograms are summarized in Table 12. The Archambeau model synthetics are somewhat longer period and lower amplitude than the elastic finite difference source synthetics. This reflects the slightly higher corner frequency produced by the finite difference source, as a result of its smaller source dimension.

The physical meaning of the important parameter stress drop is made more clear after comparing the Archambeau and elastic finite difference models. In order to scale the Archambeau source to have the same moment as the square fault model, it was necessary to make the parameter "stress drop" in the Archambeau model a factor of 3.6 smaller than that of the fault model. Thus, stress drops are under-estimated by about this amount if they are based on the Archambeau model.

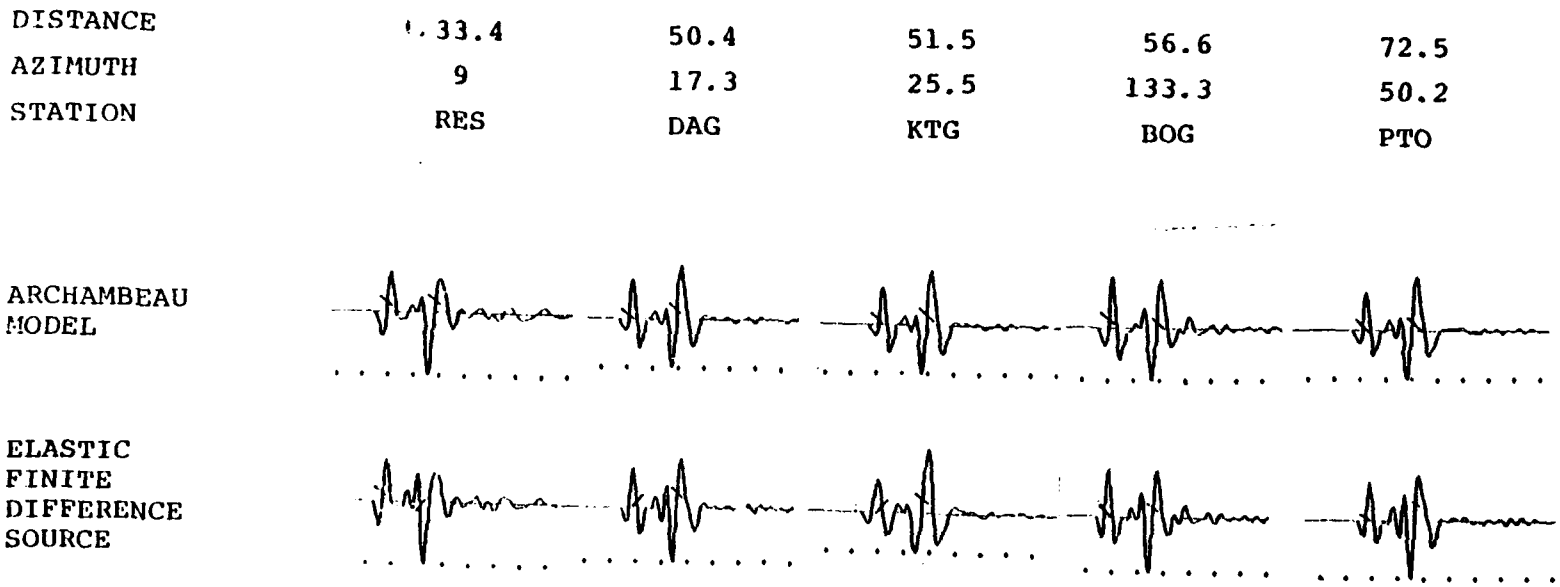

Figure 24. Comparison of synthetic seismograms from the elastic finite difference source to those from a bilateral version of the Archambeau model.

TABLE 12

AMPLITUDES AND PERIODS OF THE SEISMOGRAMS OF FIGURE 24

Stations	P PHASE		MAXIMUM PHASE		
	Amplitude (microns)	Period	Amplitude (microns)	Period	A_p/A_{max}
RES					
EFD Source*	2.11	1.1	2.59	1.0	1.23
Bi-Model I	1.84	1.3	1.96	1.2	1.07
DAG					
EFD Source	1.38	1.1	2.38	1.2	1.73
Bi-Model I	1.19	1.2	2.12	1.3	1.78
KTG					
EFD Source	1.29	1.1	2.42	1.2	1.88
Bi-Model I	1.11	1.2	2.24	1.3	2.02
BOG					
EFD Source	0.76	1.1	1.75	1.3	2.30
Bi-Model I	0.69	1.2	1.53	1.4	2.21
PTO					
EFD Source	0.67	1.1	1.96	1.3	2.93
Bi-Model I	0.61	1.2	1.88	1.4	3.08

* Elastic Finite Difference Source Model.

5.3 DISCUSSION

The inclusion of a simple form of inelastic material response was intended as a step toward developing realistic models of earthquake physics. It was found that the initial portion of the slip time-function is unaffected by the admission of a simple form of plasticity. The large velocity peak at the crack tip, characteristic of elastic crack problems, persisted in the inelastic case. The stopping phase was modified somewhat, however. Yielding at the edge of the fault resulted in less abrupt stopping, reducing the high-frequency content of both the slip function and the far-field displacements, and increasing the average slip by 11 percent. Accumulation of plastic strain beyond the fault edge resulted in a 38 percent higher moment than in the elastic case.

These effects of plasticity depend upon our choice of the magnitude of prestress, the yield strength, the frictional stress, and the dimensions of the nonlinear zone. The problem treated was an extreme case in the sense that the prestress level everywhere equaled the strength of the medium ($Y/\sqrt{3}$). With a moderate increase in the yield strength (26 percent), or a similar decrease in the prestress, there would have been no yielding, and the solution would have been identical to that of the elastic problem. On the other hand, we arbitrarily limited the extent of the plastic zone. Outside the plastic zone, a static shear stress concentration persisted which was nearly as large as that of the elastic case; had the plastic zone been larger, more plastic strain would have occurred, resulting in an even larger seismic moment.

The next step will be incorporation into the model of a fracture criterion, so that rupture advance is governed by rock strength rather than being arbitrarily prescribed. There are three requirements that we shall impose on a realistic fracture mechanism. The first two are that energy should be

dissipated at the crack tip and that stresses and velocities should remain bounded everywhere. The third requirement is that the criterion of rupture can be formulated numerically so as to be nearly zone-size dependent.

Ida (1972) has shown that, when the stress drop is abrupt, limiting the shear stress on the fault plane is not sufficient to prevent singularities in velocity and stress components. This is supported by our observation (Sections 5.2.2 and 5.2.3) that plastic yielding did not reduce peak velocities. On the other hand, Ida (1972) and Andrews (1976) have shown that a slip-weakening model, in which the stress drops gradually as a function of the relative displacement, produces bounded stresses and velocities and absorbs finite energy at the rupture front. Since the rupture front is smeared out in a slip-weakening model, it is likely to yield a rupture advance which is nearly independent of zone size.

5.4 RESEARCH PLANS

- Extend our work on faults with prescribed rupture velocity to include unilateral rupture on a long, narrow fault. We anticipate performing one, or perhaps two, elastic calculations to evaluate the effect of this geometry on the source function.

- Formulate a failure criterion in three-dimensions and develop an algorithm to be incorporated into the finite difference code.

- Exercise the rupture model in the presence of constant prestress. Relationship of the model parameters to rupture velocity, stress concentrations and slip function shape will be examined. It is anticipated that rupture growth will have to be terminated artificially in this model.

• Investigate the circumstances under which rupture growth stops spontaneously. An important mechanism may be nonuniform stress drop. Several studies based on kinematic earthquake models (for example, Bache and Barker, 1978 and Barker, et al., 1978) have indicated that variable stress drop has an important influence on the seismic radiation, particularly on the relative excitation of high- versus low-frequency signals. This should be pursued in the context of a deterministic source model, in which stress drop and rupture velocity are coupled through a failure mechanism.

VI. DISCRIMINATION EXPERIMENT

Our objective in the discrimination experiment is to analyze short-period seismic waveforms from a large population of events in order to identify the events as either earthquakes or underground explosions. During this reporting period we processed P-wave seismograms for 52 events recorded at the the classified stations.

The MARS computer program that is being used in the discrimination experiment is described in Section III. During this reporting period, two modifications were made to the procedure used for estimating the variable frequency magnitudes. One of these modifications involved the development of an algorithm for estimating the effect of "local seismic noise" on a transient signal (Masso, et al., 1978). The second modification consists of averaging weighted magnitude estimates at several different frequencies over a low (e.g., 0.6 to 0.9 Hz) and a high (e.g., 2.5 to 3.5 Hz) frequency band. The weights are based on the ratio of signal power to noise power. These weighted mean magnitudes are more stable estimates than values computed at the individual filter frequencies (Savino, et al., 1978).

In the following we will give a brief description of the changes to MARS and conclude with a narrative summary of the discrimination results obtained to date for the classified data set.

6.1 SEISMIC NOISE CORRECTION

Earlier applications of the VFM approach to discrimination included a rather crude noise correction to the $m_b(f)$ data. The particular form of this correction, namely the subtraction of a frequency dependent average noise level, was observed to

result in a biased (high) estimate of the probable noise level occurring during a signal time window. In addition, the phase of the noise relative to that of the signal was not taken into account. We have now developed, and are routinely using, a more accurate noise correction that takes advantage of the narrow-band filtering procedure (Masso, et al., 1978).

In principle, the noise correction, as now applied, consists of a deterministic component and a statistical component. The deterministic component is based on a superposed pulse model for the noise, where noise is defined as all energy or group arrivals not identified with the particular signal being considered. Given this definition, the "noise" can be made up of what would ordinarily be considered signal (e.g., the coda of the first arrival P-wave), as well as normal background seismic noise. The particular form of the correction that treats this "local seismic noise" is termed deterministic because the effects of both the amplitude and instantaneous phase of the "noise" on the signal can be calculated, at least to first order.

As described in Section III, the output of the narrow band filtering process consists of maxima of envelope functions as a function time. The deterministic noise correction is formulated as follows. Let $A_g^*(f)$ be the measured envelope amplitude associated with a signal of interest, and $t_g^*(f)$ be the energy, or group, arrival time. In addition, let $\{A_n(f)\}$ be a set of noise peaks with group times $\{t_g^N(f)\}$ such that, either: $t_g^* - \delta t \leq t_g^N(f) \leq t_g^* - \Delta t$, or $t_g^* + \Delta t \leq t_g^N(f) \leq t_g^* + \delta t$; where:

$$\delta t = \frac{10\ \ell n 2}{\Delta\omega} \quad ; \quad t = \frac{1}{2\Delta\omega}$$

and suppose that there are M such noise peaks. Here $\Delta\omega$ is the half power band width of the Gaussian filters that are used in MARS (see Section III).

We compute the "local noise corrected signal amplitude," $A_g^{**}(f)$, from:

$$A_g^{**}(f) = \left[\left\{ A_g^* \cos \psi_p^*(t_g^*) - \sum_{m=1}^{M} A_N^{(m)} \exp \left[\frac{-\Delta\omega^2}{4\beta} (t_g^* - t_g^m)^2 \right] \cdot \cos \psi_p^{(m)}(t_g^*) \right\}^2 + \left\{ A_g^* \sin \psi_p^*(t_g^*) - \sum_{m=1}^{M} A_N^{(m)} \exp \left[\frac{-\Delta\omega^2}{4\beta} (t_g^* - t_g^{(m)})^2 \right] \sin \psi_p^{(m)}(t_g^*) \right\}^2 \right]^{1/2}$$

where:

$$\beta = \frac{\ln 2}{2}$$

$\psi_p^*(t_g^*)$ ≡ Instantaneous phase of the signal at the envelope peak time (group time) $t_g^*(f)$.

$A_g^*(t_g^*)$ ≡ Amplitude of the envelope at the peak in the envelope function, occurring at $t_g^*(f)$.

$\psi_p^{(m)}(t_g^m)$ ≡ Instantaneous phase of the m^{th} "noise" pulse at the envelope peak time (group time), $t_g^m(f)$.

$\psi_p^{(m)}(t_g^*) = \omega_o(t_g^* - t_g^m) + \psi_p^{(m)}(t_g^m)$ = the noise phase at t_g^*, the <u>signal</u> group time.

$A_N^{(m)}(f)$ = Amplitude at the envelope peak for the m^{th} noise pulse (occurring at the time $t_g^m(f)$).

Here:

$$\delta A_N = \sum_{m=1}^{M} A_N^{(m)} \exp\left[\frac{-\Delta\omega^2}{4\beta}(t_g^* - t_g^m)^2\right] \cos \Psi_p^{(m)}(t_g^*)$$

is the deterministic noise correction for the signal with group time t_g^*, while

$$\delta\hat{A}_N = -\sum_{m=1}^{M} A_N^{(m)} \exp\left[\frac{-\Delta\omega^2}{4\beta}(t_g^* - t_g^m)^2\right] \sin \Psi_p^{(m)}(t_g^*)$$

is the quadrature component corresponding to δA_N. We then compute both of these and evaluate the (deterministic) noise correction $|\delta A_N|$ as:

$$|\delta A_N| = [(\delta A_N)^2 + (\delta\hat{A}_N)^2]^{1/2}$$

and save for later use in describing the noise population in the $m_b(f)$ plane. This correction, while deterministic, is only to first order.

AD-A125 834 AUTOMATED MAGNITUDE MEASURES EARTHQUAKE SOURCE MODELING 2/2
VFM DISCRIMINANT..(U) SYSTEMS SCIENCE AND SOFTWARE LA
JOLLA CA T C BACHE ET AL. FEB 79 SSS-R-79-3933
UNCLASSIFIED F08606-79-C-0008 F/G 8/11 NL

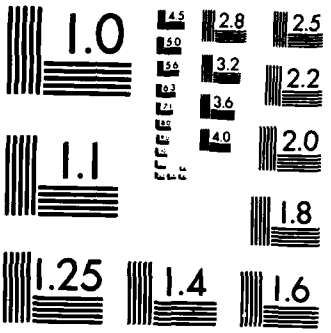

Associated with $A_g^{**}(f)$ will be an uncertainty due to the impossibility of resolving and correcting for noise peaks within the range $\Delta t = \frac{1}{2\Delta\omega}$ on either side of the signal group time (t_g^*), at a frequency f. In addition, we will want to include in the uncertainty attached to the estimate A_g^{**}, the impossibility of making an exact deterministic correction for noise contamination from the "local" noise pulses. This uncertainty will be $\pm \Delta A_N$, with ΔA_N given by:

$$\Delta A_N = \left(\frac{Q}{\omega}\right) \left(\frac{L}{T_o}\right) \bar{A}_N(f) = \frac{1}{\Delta\omega} \left(\frac{L}{T_o}\right) \bar{A}_N$$

where

T_o = Total (standard) time window being processed (typically above 100 sec).

L = Number of <u>noise</u> peaks in T_o. (Use the previously analyzed time window where all noise peaks have been identified.)

$\bar{A}_N(f)$ = Mean of the envelope amplitudes at the noise peaks in the window T_o, i.e., $\bar{A}_N(f) = \sum_{\ell=1}^{L} A_N^{(\ell)}(f)/L$.

(Note that $L \propto \Delta\omega\, T_o$ as $\Delta\omega \to 0$, so that $\Delta A_N \to \bar{A}_N$ as $\Delta\omega \to 0$. Further, $\delta A_N \to 0$ as $\Delta\omega \to 0$ by definition of the time interval for the δA_N correction. Therefore as $\Delta\omega \to 0$, and the filter Q become infinite, we get the usual noise correction of a Fourier spectrum.) Thus the signal spectral amplitude will be described by $A_g^{**}(f) \pm \Delta A_N(f)$.

The final step in this formulation is the computation of the noise corrected instantaneous phase. This is given by:

$$\Psi_P^{**}(t_g^*(f)) = +\tan^{-1}\left[\frac{\hat{y}^* - \delta\hat{A}_N}{y^* - \delta A_N}\right]$$

where δA_N and $\delta\hat{A}_N$ are as defined above while

$$y^* \equiv A_g^* \cos \Psi_P^*(t_g^*)$$

$$\hat{y}^* \equiv + A_g^* \sin \Psi_P^*(t_g^*)$$

where $\hat{y}^*$ is the quadrature signal.

6.2 NOISE CORRECTED MEAN WEIGHTED $\bar{m}_b(f)$ ESTIMATES

The application of the noise correction derived above is based on a magnitude relationship similar to the one originally proposed by Gutenberg and Richter (1956):

$$m_b(f) = \log_{10}[Af] + b$$

where b is the distance correction factor. Using this relationship we compute $m_b(f)$ values for the signal of interest from $A_g^*(f)$, $A_g^{**}(f)$, $A_g^{**}(f) + \Delta A_N$ and $A_g^{**}(f) - \Delta A_N$. The $m_b(f)$ are computed at frequencies corresponding to the center frequencies of the entire set of narrow band filters being used (i.e., typically 30 filters covering the band 0.5 to 5 Hz). For discrimination purposes, however, two sub-bands are defined: a low frequency set $\{f_L\}$, where $0.5 \leq f \leq 1.0$ Hz; a high frequency set $\{f_H\}$, where $2.5 \leq f \leq 3.5$ Hz. In order to obtain more stable magnitude estimates than those based on

individual frequencies, we are now computing mean weighted $\bar{m}_b(f)$ values over the frequency sets $\{f_L\}$ and $\{f_H\}$ and using these in the discrimination experiment. The magnitude relationship is given by:

$$\bar{m}_b(f) = \log_{10}\left[\sum_{k=1}^{N} w_k \ (A_k^{**} f_k) \Big/ \sum_{k=1}^{N} w_k\right] + b$$

where

$$w_k(f) = [A_g^*/\bar{A}_N]^2$$

are weight factors, measuring the signal information content or "quality" of the signal information at the frequency f_k. The summation is performed over the low, $\bar{m}_b(f_L)$, and high $\bar{m}_b(f_H)$, frequency discrimination sub-bands.

Associated with the magnitudes $\bar{m}_b(f_L)$ and $\bar{m}_b(f_H)$ are the frequencies $\bar{f}_L$ and $\bar{f}_H$ defined by:

$$\bar{f}_L = \sum_{k=1}^{N} w_k \ f_L^{(k)} \Big/ \sum_{k=1}^{N} w_k$$

and

$$\bar{f}_H = \sum_{k=1}^{N} w_k \ f_H^{(k)} \Big/ \sum_{k=1}^{N} w_k \quad .$$

Finally, we also compute the uncertainty in the weighted mean magnitudes at $\bar{f}_L$ and $\bar{f}_H$ due to the uncertainty in the noise correction. These are given by:

$$\Delta m_b^+(f) = \log_{10}\left[\sum_{k=1}^{N} w_k (A_k^{**} + \Delta A_N^k)\ f_k / \sum_{k=1}^{N} w_k\right]$$

$$+ b - \bar{m}_b(f)$$

$$\Delta m_b^-(f) = \log_{10}\left[\sum_{k=1}^{N} w_k (A_k^{**} - \Delta A_N^k)\ f_k / \sum_{k=1}^{N} w_k\right]$$

$$+ b - \bar{m}_b(f).$$

Note that $\Delta m_b^+ \neq -\Delta m_b^-$ in general, and that none of the Δm_b values obtained for the two sets of discrimination frequencies will be equal in general. We get from this then four distinct Δm_b values.

The results of applying the newly formulated noise correction to event $m_b(f)$ data are summarized in Figures 25a and 25b. Figure 25a shows the behavior of typical event (uncorrected for noise) and noise populations in the $m_b(f)$ plane. This figure is a generalization of earlier results previously reported on (Savino, et al., 1975; Rodi, et al., 1978). Figure 25b demonstrates the manner in which the earthquake and explosion populations separate when the deterministic and statistical noise corrections, together with the uncertainty inherent in both these corrections, are applied. The enhanced separation of populations is especially significant in the low $m_b'(f)$ range where noise plays an important role. The primed $m_b(f)$ values in Figure 25b refer to weighted mean magnitudes determined from the low and high frequency bands. This is the procedure that we are routinely using in the discrimination experiment for the computation of the variable frequency magnitudes.

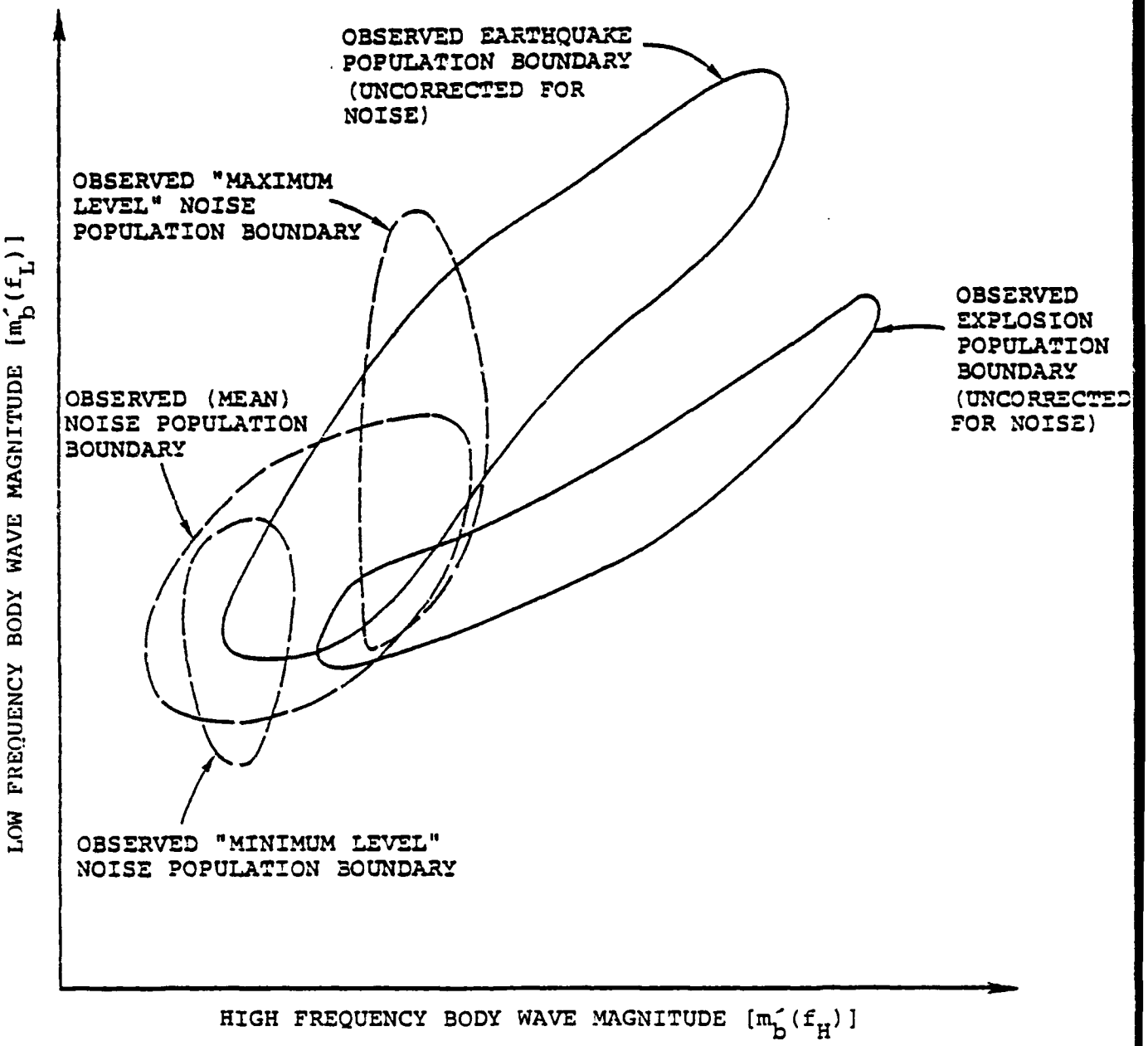

Figure 25a. Typical event distributions in the $m_b(f)$ plane for event data that is not corrected for noise contamination. Noise pulses, when viewed in this space appear roughly as shown and affect explosion event $m_b(f_L)$ values most strongly, causing population overlap at low magnitudes. The population boundaries for noise and events are somewhat source and receiver dependent due to earth structure variations.

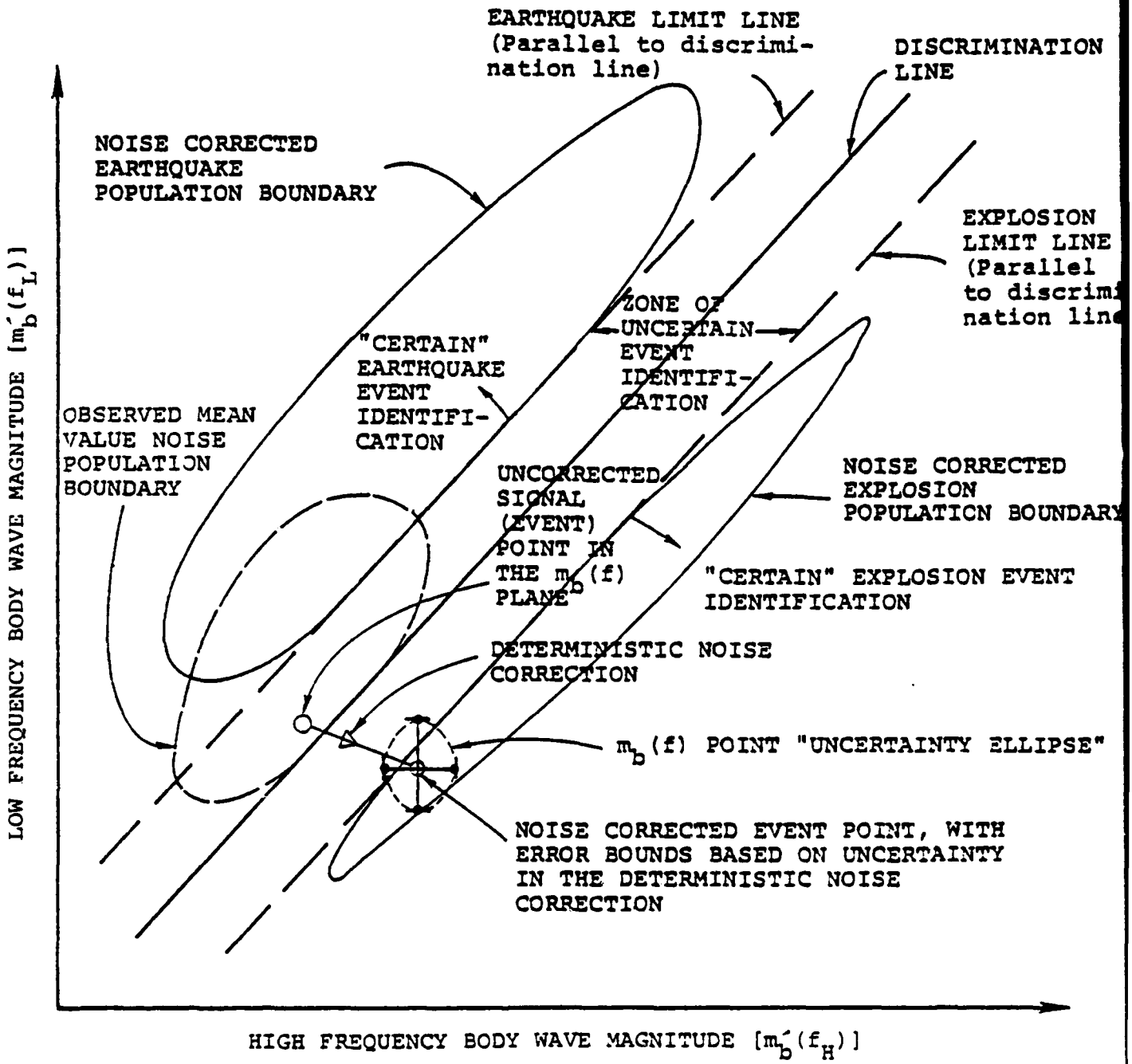

Figure 25b. Typical event distributions in the $m_b(f)$ plane for noise corrected event data. A discrimination line can be defined on the basis of the definition of these populations using known events, or on the basis of theoretical predictions.

6.3 DISCRIMINATION RESULTS

Event seismograms for 52 events recorded at one or more of the eight classified stations were received at S^3 and processed during this reporting period. Preliminary results indicate that the variable frequency magnitude (VFM) approach can discriminate events down to small magnitude levels (low P-wave signal-to-noise ratios) at those stations characterized by relatively low background noise levels. There is also a suggestion that stations located over probable high-Q upper mantle regions (e.g., shields) provide better separation of earthquakes and explosions than do stations located in tectonic regions of high heat flow and large positive (slow) travel-time residuals (by inference, low-Q upper mantle regions). These tentative results will be examined in much greater detail once the entire data base (both classified and unclassified stations) has been analyzed.

The numbers of events presently at S^3 are 92 for the classified stations and 117 for the unclassified stations. Our future plans are to first complete analysis of the classified data and then proceed to the unclassified set. The data processing (i.e., MARS runs on all the seismograms) should be completed by the end of February. Assuming a modest number of additional events, final reports on the Priority 1 and 2 station sets will be completed by mid-April.

REFERENCES

Bache, T. C. (1976), "The Effect of Tectonic Stress Release on Explosion P-Wave Signatures," BSSA, 66, pp. 1441-1457.

Bache, T. C. (1979), "$\hat{m}_b$, A Spectral Body Wave Magnitude (U)," Systems, Science and Software Report SSS-CR-79-3901, January. (S)

Bache, T. C., J. T. Cherry, N. Rimer, J. M. Savino, T. R. Blake, T. G. Barker and D. G. Lambert (1975), "An Explanation of the Relative Amplitudes Generated by Explosions in Different Test Areas at NTS," Systems, Science and Software Final Report to the Defense Nuclear Agency, DNA 3958F, October.

Bache, T. G. and D. G. Harkrider (1976), "The Body Waves Due to a General Seismic Source in a Layered Earth Model: 1. Formulation of the Theory," BSSA, 66, pp. 1805-1819.

Bache, T. C., T. G. Barker, N. Rimer and J. M. Savino (1976), "Comparison of Theoretical and Observed Body and Surface Waves for KASSERI, an Explosion at NTS," Systems, Science and Software Report SSS-R-76-2937, May.

Bache, T. C., W. L. Rodi and D. G. Harkrider (1978), "Crustal Structures Inferred from Rayleigh Wave Signatures of NTS Explosions," BSSA, 68, pp. 1399-1413.

Bolduc, P. M., R. M. Ellis and R. D. Russell (1972), "Determination of Seismograph Phase Response from the Amplitude Response," BSSA, 62, pp. 1665-1672.

Dahlman, O. and H. Israelson (1977), Monitoring Underground Nuclear Explosions, Elsevier Scientific Publishing Company, Amsterdam.

Day, S. M., T. C. Bache, T. G. Barker and J. T. Cherry (1978), "A Source Modal for the 1975 Pocatello Valley Earthquake," Systems, Science and Software Scientific Report submitted to the Air Force Geophysics Laboratory, SSS-R-79-3893, December.

Eisler, J. D. and F. Chilton (1964), "Spalling of the Earth's Surface by Underground Nuclear Explosions," J. Geophys. Res., 69, pp. 5285-5293.

Gutenberg, B. and C. F. Richter (1956), "Magnitude and Energy of Earthquakes," Ann. Geofis., 9.

Helmberger, D. V. and R. A. Wiggins (1971), "Upper Mantle Structure of the Midwestern United States," J. Geophys. Res., 76, pp. 3229-3245.

Hill, P. and C. Pakiser (1967), "Seismic-Refraction Study of Crustal Structure Between the Nevada Test Site and Boise, Idaho", Geol. Soc. of Am. Bull., 78, pp. 685-704.

Lambert, D. G., T. C. Bache and J. M. Savino (1977), "Simulation and Decomposition of Multiple Explosions", Systems, Science and Software Topical Report, AFTAC/VSC, SSS-R-77-3194, June.

Lambert, D. G. and T. C. Bache (1977), "Identification of Individual Events in a Multiple Explosion from Teleseismic Short Period Body Wave Recordings", Systems, Science and Software Technical Report, SSS-R-78-3421, October.

Masso, J. F., C. B. Archambeau and J. M. Savino (1978), "Implementation, Testing and Specification of a Seismic Event Detection and Discrimination System," Systems, Science and Software Technical Progress Report (Draft), SSS-R-79-3833, to the U. S. Arms Control and Disarmament Agency, October.

Mueller, R. A. and J. R. Murphy (1971), "Seismic Characteristics of Underground Nuclear Detonations", BSSA, 61, p. 1975.

Orkild, P. P., K. A. Sargent and R. P. Snyder (1969), "Geologic Mpa of Pahute Mesa, Nevada Test Site, Nye County, Nevada", U. S. Geol. Survey Misc. Geol. Inv. Map, I-567.

Rodi, W. L., J. M. Savino, T. G. Barker, S. M. Day and T. C. Bache (1978), "Analysis of Explosion Generated Surface Waves in Africa, Results from the Discrimination Experiment and Summary of Current Research", Systems, Science and Software Quarterly Technical Report, SSS-R-78-3653, April.

Savino, J. M. and C. B. Archambeau (1974), "Discrimination of Earthquakes from Single and Multiple Explosions Using Spectrally Defined Event Magnitudes", Trans Amer. Geophys., Union, EOS (Abstract), 56, 1148.

Savino, J. M., T. C. Bache, J. T. Cherry, K. G. Hamilton, D. G. Lambert and J. F. Masso (1975), "Application of Advanced Methods for Identification and Detection of Nuclear Explosions from the Asian Continent", Systems, Science and Software Semi-Annual Technical Report, SSS-R-76-2792 to AFOSR, December.

Savino, J. M., J. F. Masso and C. B. Archambeau (1979), "Implementation, Testing and Specification of a Seismic Event Detection and Discrimination System", Systems, Science and Software Final Contract Report to be submitted to ACDA, February.

Savino, J. M., N. Rimer, H. J. Swanger and T. C. Bache (1978), "Source Studies, Results from the Discrimination Experiment and Summary of Current Research," Systems, Science and Software Quarterly Technical Report, SSS-R-78-3736, to the Advanced Research Projects Agency, August.

Shapira, A. and O. Kulhanek (1978), "Conventional and Spectral Short Period Body-Wave Magnitudes," BSSA, 68, pp. 1195-1198.

Sobel, P. A. (1978), "The Effects of Spall on m_b and M_s," Unpublished Teledyne Geotech Report.

Springer, D. L. (1974), "Secondary Sources of Seismic Waves from Underground Nuclear Explosions", BSSA, 64, pp. 581-594.

Viscelli, J. A. (1973), "Spallation and the Generation of Surface Waves by an Underground Explosion", J. Geophys. Res., 78, pp. 2475-2487.

Woolson, J. R. (1978), Draft Memorandum Concerning Instrument Response, 11 July.

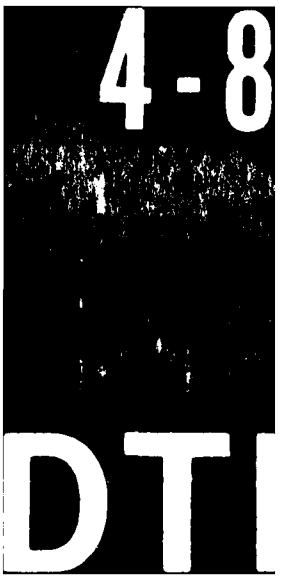
4-8
DTI